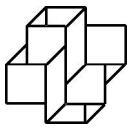

Laboratório Nacional de Computação Científica

Programa de Pós-Graduação em Modelagem Computacional

Análise da Implementação da Porta Toffoli em Sistemas com Imperfeições

Por

Jalil Khatibi Moqadam

PETRÓPOLIS, RJ - BRASIL

JANEIRO DE 2014

ANÁLISE DA IMPLEMENTAÇÃO DA PORTA TOFFOLI EM SISTEMAS COM IMPERFEIÇÕES

Jalil Khatibi Moqadam

TESE SUBMETIDA AO CORPO DOCENTE DO LABORATÓRIO NACIONAL DE COMPUTAÇÃO CIENTÍFICA COMO PARTE DOS REQUISITOS NECESSÁRIOS PARA A OBTENÇÃO DO GRAU DE DOUTOR EM CIÊNCIAS EM MODELAGEM COMPUTACIONAL

Aprovada por:

Prof. Renato Portugal, D.Sc
(Presidente)

Prof. Paulo Cesar Marques Vieira, D.Sc.

Prof. Marcos Cesar de Oliveira, D.Sc.

Prof. Reinaldo Oliveira Vianna, D.Sc.

PETRÓPOLIS, RJ - BRASIL
JANEIRO DE 2014

Khatibi Moqadam, Jalil

K45a Análise da implementação da porta Toffoli em sistemas com imperfeições / Jalil Khatibi Moqadam. Petropólis, RJ. : Laboratório Nacional de Computação Científica, 2014.

xii, 69 p. : il.; 29 cm

Orientadore(s): Renato Portugal , Nami Fux Svaiter e Gilberto Oliveira Corrêa

Tese (D.Sc.) – Laboratório Nacional de Computação Científica, 2014.

1. Computadores quânticos 2. Computação quântica 3. Teoria do controle em física matemática 4. Ruído quântico. I. Portugal, Renato. II. LNCC/MCT. III. Título.

CDD 004.1

“There is no such thing as teaching without research and research without teaching.”
(Paulo Freire)

To my wife

for her love and patience

Acknowledgment

I would like to express my thanks to Dr. Renato Portugal not only for his supervising during the preparation of this thesis but also for helping me to come to Brazil that led to a quite different invaluable experience in my life.

I also want to give my thanks to Dr. Gilberto Corréa and Dr. Nami Svaiter for their contribution to this work.

I wish to thank Dr. Paulo César and Dr. Paulo Esquef from whom I learned a lot during these years.

I acknowledge Conselho Nacional de Desenvolvimento Científico e Tecnológico (CNPq) for the PhD scholarship.

Resumo da Tese apresentada ao LNCC/MCT como parte dos requisitos necessários para a obtenção do grau de Doutor em Ciências (D.Sc.)

ANÁLISE DA IMPLEMENTAÇÃO DA PORTA TOFFOLI EM SISTEMAS COM IMPERFEIÇÕES

Jalil Khatibi Moqadam

Janeiro , 2014

Orientador: Renato Portugal, D.Sc

Co-advisors: Nami Fux Svaiter, D.Sc.

Gilberto Oliveira Corrêa, Ph.D

Neste trabalho, o desempenho da porta Toffoli sob a influência de imperfeições é estudada. Depois de dar uma breve introdução à computação quântica e teoria de controle quântico, os qubits supercondutores de tipo de carga e seus acoplamentos a um ressonador da linha de transmissão são discutidos. Em seguida, a execução da porta Toffoli numa cadeia de três qubits supercondutores de tipo transmon, utilizando métodos de controle quântico, é revisada. Tendo estabelecido a porta, o ruído é introduzido nas interações entre os qubits. As constantes de acoplamento, então, não ficam fixas, flutuam em torno de valores médios e obedecem a algumas funções de densidade de probabilidade conhecidas que caracterizam o caso da imperfeição dinâmica. O caso da imperfeição estática no qual os valores das constantes de acoplamento não são conhecidas com precisão é também considerado. Finalmente, uma porta mais robusta é projetada com uma modificação do problema de otimização quântico usando uma fidelidade média ponderada como funcional objetivo.

Abstract of Thesis presented to LNCC/MCT as a partial fulfillment of the requirements for the degree of Doctor of Sciences (D.Sc.)

ANALYZING THE IMPLEMENTATION OF THE TOFFOLI GATE IN SYSTEMS WITH IMPERFECTIONS

Jalil Khatibi Moqadam

January, 2014

Advisor: Renato Portugal, D.Sc

Co-advisors: Nami Fux Svaiter, D.Sc.

Gilberto Oliveira Corrêa, Ph.D

In this thesis, the performance of the Toffoli gate under the influence of imperfections is studied. After giving a brief introduction to quantum computing and quantum control theory, superconducting charge qubits and their couplings to the transmission line resonator are discussed. Then, the implementation of the Toffoli gate in a chain of three superconducting transmon qubits, using quantum control methods, is reviewed. Having established the gate, the noise is introduced in the interqubits interactions. The coupling constants are then no longer fixed, instead, they fluctuate around average values obeying some given probability density functions characterizing the dynamical-imperfection case. The static-imperfection case in which the values of the coupling constants are not exactly known is also considered. Finally, a more robust gate is designed by modifying the quantum optimization problem using some weighted average fidelity as the objective functional.

Contents

List of Figures

Figure

Chapter 1

Introduction

Physical implementations of quantum information processing are always subjected to various imperfections that decrease the performance of the process. Imperfections can be dynamical or static. While in dynamical imperfections the noisy parameters change their values in time with some frequencies, in static imperfections the realization of the noise parameters remain constant for a time period much larger than the time that is required to fulfill the process job.

Dynamical imperfections as a result of system-environment coupling produce decoherence in the system destroying the benefits of using quantum information. Static imperfections on the other hand do not introduce decoherence to the system yet lead to error as well.

Georgeot and Shepelyansky (2000b,a) have already considered a two dimensional lattice of qubits with nearest-neighbor interqubit couplings as a standard generic quantum computer model to incorporate imperfections. This model shows that, for a system affected by static imperfections, quantum chaos sets in above a critical interqubit strength and annihilates the quantum computer performance (Georgeot and Shepelyansky (2000a)).

Consequently, the entanglement dynamics also exhibit a transition from integrability to quantum chaos (Montangero et al. (2003); Montangero and Viola (2006)). However, the entanglement dynamics remain almost unaffected for disorders less than 10% (Tsomokos et al. (2007, 2008)).

Facchi et al. (2005) have also used the same model to study the dynamical imperfections in quantum computers. In this case a characteristic frequency is associated with the noise that is specifying the rate at which the noise changes. They have shown that for low frequencies the imperfections can be considered static, and for sufficiently high frequencies the effect of noise completely disappears.

Implementations of quantum computers specifically require high fidelity quantum gates. There are many measures for the robustness of a quantum gate against noise (see for example Harrow and Nielsen (2003)). Particularly, one- and two-qubit quantum gates that are universal for quantum computing have already been analyzed under the influence of noise (Hu and Das Sarma (2002); Paladino et al. (2011); Green et al. (2012); Bogdanov et al. (2013)).

The standard way of implementation of the multiqubit gates is to decompose them into a sequence of single- and two-qubit gates (Barenco et al. (1995)). However, the implementation of multi-qubit gates using such decompositions in terms of a universal gate set may not be efficient because the implementation time may exceed the decoherence time.

Another approach to implement multiqubit gate is to implement them directly without using the decomposition method. The Toffoli gate, a three-qubit gate with central role in quantum information processing, has been recently implemented with less resources and moderate fidelities (Monz et al. (2009); Fedorov et al. (2011); Reed et al. (2012a)). However, new proposals have been suggested to realize the Toffoli gate with fidelities above 99% (Stojanović et al. (2012); Chen et al. (2012)).

It is possible to use quantum control methods to design a set of microwave pulses to realize the Toffoli gate in a chain of three superconducting qubits which are embedded in circuit quantum electrodynamics (circuit QED) setup.

Superconducting qubits are promising candidates in constructing quantum networks to perform quantum information processing tasks. They are macroscopic prototypes of qubits which are based on Josephson tunnel junction and proved to

have quantum properties like atoms (Clarke and Wilhelm (2008); You and Nori (2011)). Superconducting qubits are coupled to microwave photons within circuit QED setup which is the on-chip implementation of the cavity quantum electrodynamics (cavity QED). It consists of a transmission line resonator playing the role of the cavity and a superconducting qubit serving as the artificial atom. The Jaynes-Cummings model describes the interaction between the photon and the qubit, when the so called rotating wave approximation is applicable (Blais et al. (2004); Schoelkopf et al. (2008)). The control and readout of the qubit state can be effectively performed using external wave generators.

The coupling between the qubits within a circuit QED is mediated by virtual exchange of photons with the cavity in the large detuning dispersive regime. In this regime, an effective qubit-qubit interaction of isotropic XY type appears when the rotating wave approximation is applicable (Blais et al. (2004, 2007); Majer et al. (2007)). Various two- and three-qubit quantum information processing tasks have already been performed with moderate fidelities using such coupling between the qubits (DiCarlo et al. (2009, 2010); Fedorov et al. (2012); Reed et al. (2012b)).

Actually in a circuit QED setup, Stojanović et al. (2012) design a sequence of microwave pulses that realizes the Toffoli gate with a fidelity above 99% in a time about 140 ns that is fast enough because the decoherence time T_2 in such systems is 10 to 20 μs.

Having design such multiqubit gates, it is crucial to analyze their efficiency under the influence of noise and possibly to improve their performance.

A bilinear Hamiltonian with XY-type Heisenberg chain for the system and Zeeman-like term for the control part is considered as the quantum control system to implement the Toffoli gate. Both parts in the Hamiltonian are subjected to noise. The effect of noise on the control fields has already been considered (Stojanović et al. (2012); Heule et al. (2010, 2011)) showing that the gate is more robust when the single control pulse duration is reduced. Actually, for a fixed gate time, increasing the noise has less of an effect on the average fidelity of the gate with

higher number of control pulses. However, the system Hamiltonian is also subjected to imperfections when the interqubit couplings are affected by the noise.

In this thesis, we consider the Toffoli gate that is proposed by Stojanović et al. (2012) and study the performance of the gate when the interqubit couplings are noisy. We consider the fidelity of the Toffoli gate under the influence of both the dynamical and the static imperfections. We also propose a method to improve the performance of the gate in the presence of noise.

In chapter 2 the ideas of quantum computing and quantum control theory are explained. After briefly reviewing the postulates of quantum mechanics, the quantum mechanical counterpart of the classical bit, the quantum bit (qubit) is described and finally the universal set of gates are introduced. The entangled and separable states are defined and the physical implementation of the quantum gates are presented thereafter. The chapter in continued with giving the ideas of quantum control theory and then the various forms of controllability explained. Some theorems that help to verifying the controllability of the quantum systems is pointed out. The chapter is ended with an explanation on the quantum optimal control theory and the bilinear model.

Chapter 3 is devoted to explaining superconducting qubits and circuit QED setup. The chapter starts with describing the Josephson junction that consists the basis of the superconducting qubits. The Hamiltonian of the single Josephson junction charge qubit is then presented and the ideas of qubits with two and three junctions are explained. As a charge qubit that is more resisted to the charge noise the transmon qubit is then described. Finally, the coupling of the superconducting qubits to a transmission line resonator are considered. It is described how to control a single qubit embedded in the circuit QED. The Hamiltonian of several qubits coupled to a single transmission line is also presented and the effective interaction between the qubits in the large dispersive regime is studied.

Having presented the required basis in chapters 2 and 3, analyzing the Toffoli gate in the presence of noise is discussed in chapter 4. The first part of the

chapter is devoted to briefly describing how the Toffoli gate is realized in a chain of superconducting qubits embedded in circuit QED setup when everything is ideal. To introduce imperfection to the system a noise model with a triangular form for the autocorrelation function and consequently a square *sinc* form for the power spectral density is described. After that the effect of the dynamical noise which is characterized by the noise frequency is studied. Actually, the behavior of the fidelity of the Toffoli gate is considered under the influence of imperfections with different noise frequencies and different noise standard deviations values. The chapter is ended with an explanation of the effects of the static noise which corresponds to a fixed noise in the system.

In chapter 5 it is investigated how to improve the fidelity when the system is affected by the static noise. Using optimal control techniques, two new set of control fields are obtained and their performance is analyzed under the influence of the noise that prove the enhanced fidelity. At the end special set of control fields is obtained that are quite independent from the noise in the interqubit couplings.

The conclusion and future works is presented in chapter 6.

Chapter 2

Quantum Computing and Quantum Control Theory

In this chapter the bases of quantum computing and quantum control theory are briefly reviewed. The postulates of quantum mechanics, the ideas of qubit and quantum gates are described in section 2.1. The definition of entanglement is then given and finally the physical implementation of quantum gates are described. Section 2.2 is devoted to explaining the ideas of quantum control theory. Various forms of controllability are described and some theorems are given thereafter that help to verify the controllability of the quantum systems. The section is finished with explaining the optimal control methods in bilinear systems.

The postulates of quantum mechanics that are described in this chapter as well as the ideas of quantum computing is mainly based on Nielsen and Chuang (2010). The definitions of entangled and separable states are extracted from the reference Vedral (2006). In writing the section of physical implementation of quantum gate Le Bellac (2006) and Lambropoulos and Petrosyan (2007) have been used. The quantum control section is mainly based on d'Alessandro (2008) and Machnes et al. (2011).

2.1 Quantum computing

In this section, first the general framework of quantum mechanics is reviewed and then the ideas of quantum information theory are briefly described.

The state space of a quantum system is described by a Hilbert space $\mathcal{H}$. The state of the system is completely described by a unit vector $|\psi\rangle$ in the corresponding Hilbert space. The time evolution of the state of a closed quantum system is described by the Schrödinger equation

$$\frac{d}{dt}\psi(t) = -\frac{i}{\hbar}H\psi(t), \tag{2.1}$$

where H is the Hamiltonian of the system, $\hbar$ is the Planck's constant and $i = \sqrt{-1}$ is the imaginary unit.

Considering that the Hamiltonian of the system is a Hermitian operator, the time evolution of a closed quantum system is described by a unitary transformation. In the case of time-independent Hamiltonian, the Eq. (2.1) has the solution

$$|\psi(t)\rangle = U(t)|\psi(0)\rangle; \;\; U(t) = e^{-\frac{i}{\hbar}Ht}, \tag{2.2}$$

where $|\psi(0)\rangle$ is the state of the system at $t = 0$.

Having specified the state of the system and its evolution, the next step is to measure the system. Quantum measurements are described by a collection $\{M_m\}$ of positive operators acting on the state space of the system being measured. The operators $\{M_m\}$ satisfy the completeness equation

$$\sum_m M_m^\dagger M_m = I_{\mathcal{H}},$$

where the index m refers to the measurement outcomes that may occur in the experiment and $\dagger$ represents the conjugate transpose. If the state of the quantum system is $|\psi\rangle$ immediately before the measurement, then the probability of occurrence the result m is given by

$$p(m) = \langle\psi|M_m^\dagger M_m|\psi\rangle,$$

and the state of the system after the measurement is

$$\frac{M_m|\psi\rangle}{\sqrt{p(m)}}.$$

Here, the product $\langle\ .\ |\ .\ \rangle : \mathcal{H} \times \mathcal{H} \to \mathbb{C}$ is the corresponding Hilbert space inner product.

The last point about the quantum systems which must be mentioned is the way that the compound systems are described. The state space of a composite quantum system is the tensor product of the state spaces of the component systems. The state of the system is given by the tensor product of the states of the individual subsystems.

The above statements are the postulates of quantum mechanics upon which the theory is constructed. However, the state of a physical system is often not perfectly determined. It is only known that the state of the system belongs to the ensemble

$$\{|\psi_1\rangle, |\psi_2\rangle, ..., |\psi_l\rangle\},$$

with probabilities

$$\{p_1, p_2, ..., p_l\},\ \ \sum_j p_j = 1.$$

In this case, the density operator ρ, defined by

$$\rho = \sum_l |\psi_j\rangle\langle\psi_j|, \tag{2.3}$$

is introduced. The density operator ρ is a positive operator with unit trace. The previous postulates can also be formulated in terms of the density operator to describe the ensembles. Such a formulation is mathematically equivalent to the state vector approach, but provides a more convenient way for dealing with ensembles.

With the above background on quantum mechanics the ideas of quantum information theory are described in the next paragraphs.

Quantum information theory is the generalization of classical information

theory to the quantum world. Basically, it deals with the use of quantum systems to store information, which is then processed by quantum dynamical laws.

In this thesis, only finite dimensional quantum systems are considered hence the corresponding Hilbert space is always a complex vector space equipped with the usual inner product. The quantum counterpart of the bit in the classical information theory is the qubit (quantum bit) that is a two-level quantum system, whose state is given by

$$|\psi\rangle = \alpha|0\rangle + \beta|1\rangle, \quad |\alpha|^2 + |\beta|^2 = 1, \quad \alpha, \beta \in \mathbb{C} \tag{2.4}$$

belonging to $\mathcal{H} = (\mathbb{C}^2, \langle . , . \rangle)$, being $\{|0\rangle, |1\rangle\}$ a basis for the Hilbert space $\mathcal{H}$.

A qubit can assume any of a continuum of states given by the linear superposition (2.4) suggesting an infinite information content. However, this is not the case since the result of the measurement of the qubit is restricted to $|0\rangle$ and $|1\rangle$ with the corresponding probabilities $|\alpha|^2$ and $|\beta|^2$.

The quantum counterparts of logical gates in classical computing are unitary operators. Universal gates in quantum computing are those unitary operators from which any other unitary operator over n qubits, $U \in U(2^n)$, can be constructed. It can be proved that the collection of single-qubit gates

$$U(\theta, \phi) = \begin{pmatrix} \cos\theta & ie^{i\phi}\sin\theta \\ ie^{-i\phi}\sin\theta & \cos\theta \end{pmatrix}, \quad \theta, \phi \in \mathbb{R}, \tag{2.5}$$

and the two-qubit controlled-Not gate

$$CNOT = \begin{pmatrix} 1 & 0 & 0 & 0 \\ 0 & 1 & 0 & 0 \\ 0 & 0 & 0 & 1 \\ 0 & 0 & 1 & 0 \end{pmatrix} \tag{2.6}$$

are universal (Barenco et al. (1995)).

An important gate that is used in chapter 4 is the three-qubit Toffoli gate

$$U_{\text{Toff}} = \begin{pmatrix} 1 & 0 & 0 & 0 & 0 & 0 & 0 & 0 \\ 0 & 1 & 0 & 0 & 0 & 0 & 0 & 0 \\ 0 & 0 & 1 & 0 & 0 & 0 & 0 & 0 \\ 0 & 0 & 0 & 1 & 0 & 0 & 0 & 0 \\ 0 & 0 & 0 & 0 & 1 & 0 & 0 & 0 \\ 0 & 0 & 0 & 0 & 0 & 1 & 0 & 0 \\ 0 & 0 & 0 & 0 & 0 & 0 & 0 & 1 \\ 0 & 0 & 0 & 0 & 0 & 0 & 1 & 0 \end{pmatrix} \tag{2.7}$$

which belongs to the unitary group $U(2^3)$. The Toffoli gate can be decomposed into six $CNOT$ gates and several single-qubit gates (Nielsen and Chuang (2010)).

The basic idea of quantum computation is the application of a sequence of designed unitary transformations on a collection of qubits that are prepared in known initial states and performing designed measurements on the final qubit states (DiVincenzo et al. (2000)).

2.1.1 Entanglement

The tensor product description of the composite systems in quantum mechanics makes a departure from the classical realm where the composite systems are described by the Cartesian product of the individual subsystem states. The Hilbert space of a quantum n-partite system is given by $\mathcal{H} = \otimes_{j=1}^{n} \mathcal{H}_j$, where $\mathcal{H}_j$ are the Hilbert spaces of the individual subsystems and $\otimes$ is the tensor product operation. The general state of the system is then written as

$$|\psi\rangle = \sum_{\mathbf{i}_1,\mathbf{i}_2,\ldots\mathbf{i}_n} c_{\mathbf{i}_1,\mathbf{i}_2,\ldots\mathbf{i}_n} |\mathbf{i}_1\rangle \otimes |\mathbf{i}_2\rangle \otimes \ldots \otimes |\mathbf{i}_n\rangle, \tag{2.8}$$

where $|\mathbf{i}_j\rangle$ correspond to the bases of individual subsystems and $c_{\mathbf{i}_1,\mathbf{i}_2,\ldots\mathbf{i}_n} \in \mathbb{C}$. The state (2.8) cannot in general be decomposed as a product of states of individual

subsystems

$$|\psi\rangle \neq |\psi_1\rangle \otimes |\psi_2\rangle \otimes ... \otimes |\psi_n\rangle. \tag{2.9}$$

Such states of multipartite systems for which it is not possible to assign a single state vector to individual subsystems are called entangled states.

A mixed state of a multipartite system is called entangled if it cannot be written as a convex combination of product states (density operators)

$$\rho \neq \sum_j p_j \rho_1^j \otimes \rho_2^j \otimes ... \otimes \rho_n^j. \tag{2.10}$$

The states that are not entangled are called separable. In practice, it is hard to decide if a given state is separable or entangled (Horodecki et al. (2009)).

Entanglement is a physical resource like energy, that is, associated with non-classical correlations between the quantum systems. Entangled states plays a crucial role in quantum error correction and quantum communication (Horodecki et al. (2009)).

The two-qubit $CNOT$ gate and the three-qubit Toffoli gate that are described in the previous section can produce entanglement between the qubits. Such gates cannot be decomposed as a tensor product of single qubit gates over the individual qubits. In the next section it is described how to implement such entangling gates.

2.1.2 Physical Implementation of Quantum Gates

Two-level quantum mechanical systems can be manipulated by electromagnetic fields to realize the Rabi oscillations that provide the single qubit gates. The interaction between a two-level atom with an electromagnetic field whose energy is equal the energy splitting of the two levels is given by the Hamiltonian

$$\mathcal{H} = \frac{-\hbar\Omega}{2} \begin{pmatrix} 0 & e^{i\phi} \\ e^{-i\phi} & 0 \end{pmatrix}, \tag{2.11}$$

where ϕ is the phase of the electromagnetic field and Ω is the so-called Rabi frequency. The time evolution of the Hamiltonian (2.11) is then calculated as

$$U(t) = \exp\left\{(\frac{-it}{\hbar})\frac{-\hbar\Omega}{2}\begin{pmatrix} 0 & e^{i\phi} \\ e^{-i\phi} & 0 \end{pmatrix}\right\} = \begin{pmatrix} \cos\frac{\theta}{2} & ie^{i\phi}\sin\frac{\theta}{2} \\ ie^{-i\phi}\sin\frac{\theta}{2} & \cos\frac{\theta}{2} \end{pmatrix}, \qquad (2.12)$$

where $\theta = \Omega t$. The unitary evolution (2.12) is a general qubit operation (see Eq. 2.5) that can be realized through adjusting the phase ϕ of the electromagnetic field and the time duration $t = \theta/\Omega$ when the atom is irradiated.

The two-qubit $CNOT$ gate produces entanglement between the qubits. This gate can not be decomposed as a tensor product of two single qubit operations. It is possible to realize $CNOT$ between two qubits when the two qubits are coupled together. As an example consider the following Ising interaction between two qubits

$$\mathcal{H} = -\hbar J\sigma_{1z}\sigma_{2z} \qquad (2.13)$$

where J is the coupling constant and σ_z is the Pauli Z matrix given by

$$\sigma_z = \begin{pmatrix} 1 & 0 \\ 0 & -1 \end{pmatrix}. \qquad (2.14)$$

Defining the following single qubit gates

$$R_z(\pi/2) = \frac{1}{\sqrt{2}}\begin{pmatrix} 1-i & 0 \\ 0 & 1+i \end{pmatrix}, \quad H = \frac{1}{\sqrt{2}}\begin{pmatrix} 1 & 1 \\ 1 & -1 \end{pmatrix}, \qquad (2.15)$$

the following sequence

$$I \otimes H \ . \ \exp(i\frac{\pi}{4}\sigma_z \otimes \sigma_z) \ . \ R_z(\pi/2) \otimes R_z(\pi/2) \ . \ I \otimes H, \qquad (2.16)$$

is equal to a $CNOT$ gate up to a general phase factor. Here, the first slot corresponds to the first qubit and the second slot to the second qubit. In Eq. (2.16),

the term $\exp(i\frac{\pi}{4}\sigma_z \otimes \sigma_z)$ corresponds to the evolution of the Hamiltonian (2.13) during the time $t = \pi/4J$.

Having constructed the general single qubit operations and the $CNOT$ gate, it is possible theoretically to implement any multiqubit gate. However, the implementation of the multiqubit gates using the standard decompositions in terms of the universal gates may not be efficient because the implementation time may exceed the decoherence time. Actually, before finishing the complete sequence of single and two qubit gates, the qubits interact with the environment and the quantum information are destroyed.

Another approach to implement multiqubit gate is to implement them directly by designing a sequence of electromagnetic pulses that affected the qubits individually and implement the desired gate. In this way, locally manipulating the qubits leads to generating entanglement that is mediated by the coupling between the qubits. In chapter 4 it is described how to implement the Toffoli gate using designed electromagnetic pulses. Such pulse shaping techniques involved quantum optimal control methods that are described in the next section.

2.2 Quantum Control Theory

In this section the ideas of quantum control theory is described. Pure state controllability, operator controllability and density matrix controllability are described and the corresponding theorems are then explained. Finally, optimal control theory and the bilinear model that is used for handling the quantum control problems are described.

Basically, quantum control theory deals with controlling quantum systems whose behavior is governed by the laws of quantum mechanics. This is not a trivial task because quantum systems have some unique characteristics such as entanglement for which there is no classical counterpart.

Like classical systems, it is possible to realize both the open-loop and the closed-loop control paradigms in quantum systems. In the open-loop quantum

control, predetermined controlling actions are applied to the system and no feedback is involved. In the closed-loop quantum control in contrast, the controlling actions depend on the information gained from the system hence it is called feedback quantum control (Brif et al. (2010)).

Moreover it is possible to distinguish between two different kinds of closed-loop quantum control. The distinction originates from the type of information the controller gains from the system. When the information is classical, some kind of measurement is involved and the scheme is called measurement feedback quantum control. It is also possible to use a quantum controller obtaining quantum information from the system. In this case the system undergoes (nondestructive) unitary operations. This type of control is called quantum feedback quantum control or coherent feedback control. It may be mentioned there is no classical counterpart for this type of quantum control scheme (Brif et al. (2010)).

Two main objectives of quantum control are quantum state engineering and quantum operator engineering. In quantum state engineering the aim is to steer the system from an initial state ψ_i (ρ_i) to a final state ψ_f (ρ_f). In operator control, one wish to implement a predetermined operator U irrespective of the initial state of the system.

Having established the quantum control system, one needs to know about the controllability of the system. The controllability of the system is associated with the ability to steer the system from any initial state in the corresponding Hilbert space to any other state in that space by using the admissible controllers. In the next section, the state and operator controllability are described in more details.

2.2.1 Controllability

A fundamental notion in quantum control theory is the controllability of a given quantum system. Here, some results on the controllability of *closed* quantum systems with open-loop control are presented. The results for *open* quantum

systems is given thereafter. It is more convenient to set $\hbar = 1$ which is equivalent to change the units.

Definition 1. (Pure State Controllability) The Schrödinger equation

$$\frac{d}{dt}\psi(t) = -iH(u(t))\psi(t), \tag{2.17}$$

is pure state controllable if for every pair of initial and final states, ψ_0 and ψ_1, there exist control functions u and a time $T > 0$ such that the solution $\psi(t)$ of equation (2.17) at time T, with initial condition ψ_0, is $\psi(T) = \psi_1$. Here, $u(t)$ is assumed to belong to the space of real-valued functions, $\mathcal{U}$.

Definition 2. (Operator Controllability) The Schrödinger operator equation

$$\frac{d}{dt}U(t) = -iH(u(t))U(t), \tag{2.18}$$

is operator controllable if for every unitary operator $U_f \in U(n)$ with n being the corresponding dimension of Hilbert space, there exist control functions u and a time $T > 0$ such that the solution $U(t)$ of equation (2.18) at time T, with initial condition $U(0) = I$, is $U(T) = U_f$.

Definition 3. (Density Matrix Controllability) The Liouville equation

$$\frac{d}{dt}\rho(t) = -i[H(u(t)), \rho(t)], \tag{2.19}$$

is density matrix controllable if, for each pair of unitarily equivalent density matrix ρ_1 and ρ_2, there exist control functions u and a time $T > 0$ such that the solution $\rho(t)$ of equation (2.19) at time T, with initial condition ρ_1, satisfies $\rho(T) = \rho_2$.

The following theorems give the criteria to verify the controllability of the equations (2.17−2.19).

Theorem 1. *The Schrödinger equation (2.17) is pure state controllable if and only if the Lie algebra $\mathcal{L}$ generated by span$\{-iH(u), u \in \mathcal{U}\}$ satisfies one of the followings*

1. $\mathcal{L} = u(n)$
2. $\mathcal{L} = su(n)$
3. $\mathcal{L} = span\{iI_{n\times n}\} \oplus \tilde{\mathcal{L}}$
4. $\mathcal{L}$ *is conjugate to* $sp(\frac{n}{2})$

where n *is the dimension of the corresponding Hilbert space,* $u(n)$ *is the Lie algebra of anti-Hermitian* $n \times n$ *matrices,* $su(n)$ *is the Lie algebra of zero trace anti-Hermitian* $n \times n$ *matrices,* $sp(\frac{n}{2})$ *is the symplectic Lie algebra,* $\tilde{\mathcal{L}}$ *is a Lie algebra conjugate to* $sp(\frac{n}{2})$ *and* $\oplus$ *denotes the direct sum between the Lie algebras.*

Theorem 2. *The Schrödinger operator equation (2.18) is operator controllable if and only if the Lie algebra* $\mathcal{L}$ *generated by* $span\{-iH(u), u \in \mathcal{U}\}$ *satisfies one of the followings*

1. $\mathcal{L} = u(n)$
2. $\mathcal{L} = su(n)$.

Theorem 3. *The Liouville equation (2.19) is density matrix controllable if and only if it is operator controllable.*

The set of all operators that can be reached through the system (2.18), the reachable set, is the connected Lie group $\mathcal{R}$ associated with the Lie algebra $\mathcal{L}$ as

$$\mathcal{R} = e^{\mathcal{L}}.$$

Therefore when the system is operator controllable, according to **Theorem 2** $e^{\mathcal{L}} = U(n)$ or $e^{\mathcal{L}} = SU(n)$, where $U(n)$ and $SU(n)$ denote the unitary and special unitary Lie groups respectively.

As mentioned above, **Definitions 1**, **2** and **3** and their corresponding theorems are just applied to closed quantum systems with open-loop control. For open quantum systems, the following Liouville equation describes the dynamics

$$\frac{d}{dt}\rho(t) = -i[H(u(t)), \rho(t)] + \mathfrak{L}\rho(t), \tag{2.20}$$

where $\mathfrak{L}$ corresponds to non-Hermitian superoperators representing interactions with the environment. In this case, the pure state controllability (**Definition 1**) makes no sense as the set of pure states is not invariant under non-Hermitian operations. Operator controllability (**Definition 2**) may be extended to this case by replacing unitary operators with *completely positive* maps. Density matrix controllability (**Definition 3**) is also defined for open quantum systems as before without the constraint of unitarily equivalence controllability. However the controllability of open quantum systems is still an open problem.

For closed-loop control, it has been shown that it is generally more powerful than open-loop control, especially for open quantum systems.

The controllability theorems do not usually provide constructive methods to design control laws. A very powerful tool to achieve quantum control objectives is optimal control techniques that is described in the following section.

2.2.2 Optimal Control

It is possible to formulate a quantum control task as an optimal control problem. In this approach the objective is to find admissible control functions $u(t)$ such that satisfy the system dynamics equations and simultaneously optimize an objective functional. The quantum optimal problem may be considered as minimizing the control time, minimizing the control energy, maximizing the fidelity between the final states (operator) and the target states (operator), or a combination of such requirements. A general objective functional can be written as

$$J(u) = \phi(\psi(T), T) + \int_0^T L(\psi(t), u(t), t)dt, \tag{2.21}$$

where T is the control time and ϕ and L are some smooth functions with proper domains. The minimum time problems may be associated with the first term while minimizing the energy during the control action may be formulated like the second term.

Quantum control problems can be formulated as a bilinear control system

and then the optimal control techniques can be applied to solve the problem. In the followings the bilinear method is described.

2.2.3 Bilinear Model

The dynamics of the quantum system in the bilinear model is governed by the following Hamiltonian

$$H(t) = H_0 + H_c(t), \tag{2.22}$$

where H_0 is the free (without control) system Hamiltonian and

$$H_c(t) = \sum_{k=1}^{M} u_k(t) H_k, \tag{2.23}$$

is the control Hamiltonian. Here, H_k are time independent Hermitian Hamiltonians and $u_k(t) \in \mathbb{R}$ are called control fields.

The controllability of the system can be checked through observing the Lie algebra $\mathcal{L}$ generated by the set $\text{span}\{-iH_0, -iH_k; k = 1, ..., M\}$ and considering the theorems given in section 2.2.1.

In the following, it is described how to obtain the control fields $u_k(t)$ that realize an specified target operator in a closed quantum system. Using the bilinear model, Eq. (2.18) is written as

$$\dot{U}(t) = -i \left(H_0 + \sum_{k=1}^{M} u_k(t) H_k \right) U(t), \tag{2.24}$$

with the formal solution

$$U(t) = \mathcal{T} \exp \left\{ - \int_0^{t'} dt' (H_0 + \sum_{k=1}^{M} u_k(t') H_k) \right\}, \tag{2.25}$$

where $\mathcal{T}$ denotes the Dyson's time ordering operator. As the objective functional, the following fidelity can be defined

$$F(\mathbf{u}) = \frac{1}{N} \left| \text{ Tr} \left[U_{\text{target}}^{\dagger} U(T) \right] \right|, \tag{2.26}$$

where $\mathbf{u}$ is the concatenation of all u_k and T is the total control time. The fidelity in Eq. (2.26) is actually an special case of the objective functional Eq. (2.21). The optimization problem is therefore expressed as

$$\max_{\mathbf{u}} F(\mathbf{u}). \tag{2.27}$$

In the simplest case the control fields are considered piecewise constant functions of time and the control time is divided into equal pieces accordingly. Eq. (2.24) can then be solved easily in each time interval. The total time evolution operator is obtained by multiplying the partial time evolution operators in the reverse order. Starting by an initial guess for the piecewise constant control fields, The values of the control pulses are improved through solving the optimization problem (2.27) using for example the second order method Broyden-Fletcher-Goldfarb-Shano (BFGS) (Nocedal and Wright (2006)).

In chapter 4 it is described how to apply the above model to find a set of control fields that implement the Toffoli gate in a chain of three superconducting qubits.

Chapter 3

Superconducting Qubits and Circuit Quantum Electrodynamics

In this chapter superconducting charge qubits are described and their coupling to the transmission line resonator discussed. In section 3.1 the Josephson junction which consists the basis of the superconducting qubits is explained. Using Josephson junction it is possible to realize three basic types of superconducting qubits; charge, flux and phase qubits. However, just the charge qubits are considered here, and are described in section 3.2. The transmon qubit which is a variation of the charge qubit but with a less sensitivity to the charge noise is then introduced. Finally, in section 3.3, the coupling of the superconducting charge qubits to the transmission line resonator is considered. Using Such a setup it is possible to manipulate the single qubit as well as to couple multiple qubits to realize multiqubit gates.

In writing the section of Josephson junction and superconducting charge qubits Makhlin et al. (2001) has been used as the main reference. The section for transmon qubit is based on the work of Koch et al. (2007). The material for circuit QED have been extracted from Blais et al. (2004) and Blais et al. (2007).

3.1 Josephson Junction

The state of a superconductor is described by a global wave function $\psi(\mathbf{r})$ that can be written as

$$\psi(\mathbf{r}) = |\psi(\mathbf{r})|e^{i\theta(\mathbf{r})}, \tag{3.1}$$

where $|\psi(\mathbf{r})|^2$ is the Cooper pair (electron pair) density at the position $\mathbf{r}$ and $\theta(\mathbf{r})$ is the phase of the wave function. The electromagnetic current associated with the Cooper pairs under the influence of the magnetic field $\mathbf{B}(\mathbf{r})$ that is derived from a vector potential $\mathbf{A}(\mathbf{r})$ ($\mathbf{B} = \nabla \times \mathbf{A}$) is given by

$$\mathbf{J} = \frac{2e}{m}|\psi|^2(\hbar\nabla\theta - 2e\mathbf{A}), \tag{3.2}$$

where e and m are the electron charge and mass.

By substituting the current given in Eq. (3.2) into the Maxwell equation $\nabla \times \mathbf{B} = \mu_0\mathbf{J}$, it can be shown that the magnetic field cannot penetrate the bulk of the superconductor but decreases exponentially from its surface (Meissner effect). An important consequence of the absence of the current inside the bulk of the superconductor is the quantization of the magnetic flux Φ that passes through a superconducting ring. Actually, such a flux can be written as $\Phi = n\Phi_0$ where $\Phi_0 = h/2e$ is the flux quantum and n is an integer.

A Josephson junction is made of two superconductors that are separated by a thin layer of insulating material (see Fig. 3.1). The corresponding wave functions in different sides can be coupled due to the tunneling of Cooper pairs between the two superconductors. Consequently, the so-called Josephson current

$$I = I_c \sin\varphi, \tag{3.3}$$

is created across the junction. Here, φ is the phase difference between the two wave functions and I_c is the so-called critical current, that is the maximum current that can be passed through the junction through tunneling. Moreover, the phase

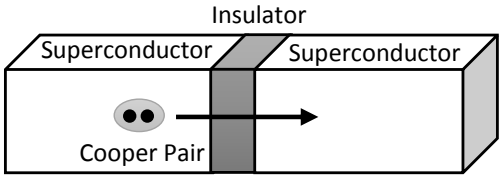

Figure 3.1: A Josephson junction consists of two superconductors that are separated by a thin layer of insulating material. The super current is created due to the phase difference between the two wave functions in different sides.

difference across the junction evolves according to

$$\frac{d\varphi}{dt} = \frac{2\pi}{\Phi_0} V, \tag{3.4}$$

where V is the voltage across the junction.

The energy stored in an ideal Josephson junction is calculated as

$$U_J = \int IV dt = \frac{I_c \Phi_0}{2\pi} \int \sin\varphi d\varphi = E_J(1 - \cos\varphi), \tag{3.5}$$

where $E_J = I_c\Phi_0/2\pi$ is called the Josephson energy.

A Josephson junction can be considered as a nonlinear inductor whose inductance can be obtained by using Eqs. (3.3) and (3.4)

$$L_J = \frac{V}{dI/dt} = \frac{V}{I_c \cos\varphi d\varphi/dt} = \frac{\Phi_0}{2\pi I_c \cos\varphi}. \tag{3.6}$$

A physical Josephson junction moreover consists of a capacitance element with corresponding capacity C_J and the charging energy E_C (see Fig. 3.2).

Superconducting qubits are constructed using Josephson junctions. Three basic kinds of superconducting qubits, can be realized where in each case the physical nature of the quantum states are different. They are charge qubits, flux qubits and phase qubits. In this thesis just the charge qubits are considered and are described in the next section.

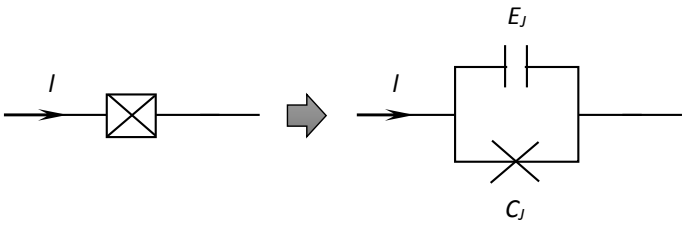

Figure 3.2: The circuit symbol for the Josephson junction is a cross inside a box that indicates a physical Josephson junction consists of both the inductance and the capacitance elements.

3.2 Superconducting Charge Qubits

The simplest superconducting *charge qubit* consists of a superconducting box that is coupled to a superconducting electrode via a Josephson junction. The system is also coupled to a control gate voltage V_g via a gate capacitor C_g. The circuit of the charge qubit is depicted in Fig. 3.3. The Hamiltonian of the system can be written as

$$\mathcal{H} = E_C(\hat{n} - n_g)^2 - E_J \cos\hat{\varphi}, \tag{3.7}$$

where

$$E_C = \frac{(2e)^2}{2(C_J + C_g)},$$

is the electrostatic energy of the capacitors and the dimensionless gate charge $n_g = C_g V_g/2e$ accounts for the gate voltage and acts as a control parameter. The operators $\hat{n}$ and $\hat{\varphi}$ are the number operator of the excess cooper pairs in the box and the junction phase difference operator, respectively. The operators $\hat{n}$ and $\hat{\varphi}$ are canonical conjugate quantities and satisfy the canonical commutation relation $[\hat{n}, \hat{\varphi}] = -i\mathcal{I}$. In the charge basis $\{|n\rangle\}$, where $\hat{n}|n\rangle = n|n\rangle$, the Hamiltonian can be written as

$$\mathcal{H} = \sum_n \left\{ E_C(n - n_g)^2 |n\rangle\langle n| - \frac{1}{2} E_J(|n\rangle\langle n+1| + |n+1\rangle\langle n|) \right\}. \tag{3.8}$$

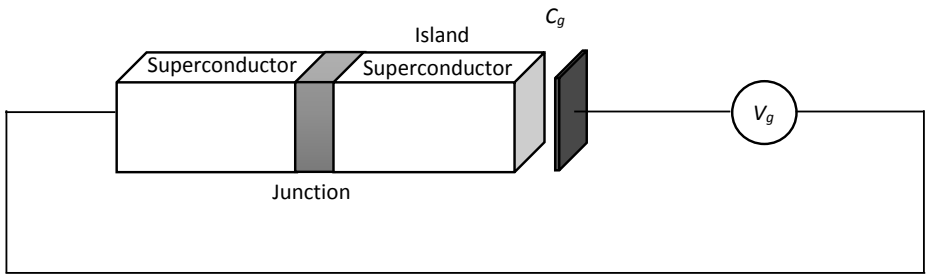

Figure 3.3: A schematic representation of the charge qubit.

Here, it is assumed that the charging energy is much larger than the Josephson energy, $E_C \gg E_J$, the so-called charging regime. Therefore, the first term in the Hamiltonian (3.8) is dominant except when n_g is close to a half integer number. Considering the case $n_g \simeq 1/2$, the energy splitting between the first two levels is of order of E_J. The higher energy states however are well separated from the two lowest energy states hence can be ignored while concentrating around the degeneracy point $n_g = 1/2$. Figure 3.4 shows the energy of the first two levels in terms of the gate charge n_g. The Hamiltonian (3.8) can then be written as

$$\mathcal{H} = E_C(n_g)^2|0\rangle\langle 0| + E_C(1-n_g)^2|1\rangle\langle 1| - \frac{1}{2}E_J(|0\rangle\langle 1| + |1\rangle\langle 0|), \tag{3.9}$$

where in the language of spin-1/2 systems in terms of the Pauli matrices it takes the form

$$\mathcal{H} = -\frac{1}{2}B_z\sigma_z - \frac{1}{2}B_x\sigma_x, \tag{3.10}$$

where $B_z = E_C(1-2n_g)$ and $B_x = E_J$ are the bias energy and the tunneling amplitude, respectively. The Pauli Z and X matrices are given by

$$\sigma_z = \begin{pmatrix} 1 & 0 \\ 0 & -1 \end{pmatrix}, \quad \sigma_x = \begin{pmatrix} 0 & 1 \\ 1 & 0 \end{pmatrix}.$$

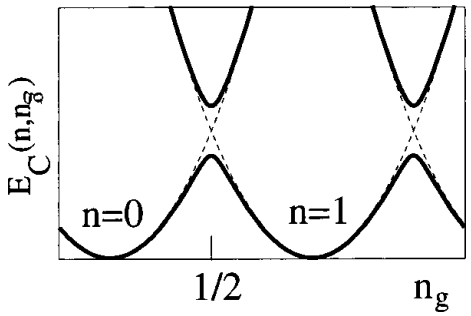

Figure 3.4: The charging energy of the first two levels of a superconducting box as a function of the gate charge n_g for different numbers of the extra Cooper pairs n in the box [source: Makhlin et al. (2001)].

The Hamiltonian (3.10) corresponds to a two-state quantum system (qubit) whose basis states are the charge states $n = 0$ and $n = 1$ that can be represented as

$$|0\rangle = \begin{pmatrix} 1 \\ 0 \end{pmatrix}, \quad |1\rangle = \begin{pmatrix} 0 \\ 1 \end{pmatrix}.$$

The eigenstates of the Hamiltonian (3.10) are denoted by $|\uparrow\rangle$ and $|\downarrow\rangle$ and calculated as

$$\begin{cases} |\uparrow\rangle = & \cos\frac{\eta}{2}|0\rangle + \sin\frac{\eta}{2}|1\rangle \\ |\downarrow\rangle = & -\sin\frac{\eta}{2}|0\rangle + \cos\frac{\eta}{2}|1\rangle \end{cases}, \tag{3.11}$$

where $\eta = \tan^{-1}(B_x/B_z)$. The energy splitting between the eigenstates is given by

$$\hbar\Omega = \sqrt{B_x^2 + B_z^2} = E_J/\sin\eta, \tag{3.12}$$

where at the degeneracy point, $n_g = 1/2$ ($\eta = \pi/2$) reduces to E_J. In the new basis $\{|\uparrow\rangle, |\downarrow\rangle\}$ the Hamiltonian (3.10) can be written as

$$\mathcal{H} = -\frac{1}{2}\hbar\Omega\overline{\sigma_z}, \tag{3.13}$$

where $\overline{\sigma_z}$ is the Pauli Z matrix in the new basis.

The bias energy B_z in the system (3.10) can be controlled by playing with the gate voltage n_g. However, the tunneling energy B_x has a constant value that

depends on the Josephson energy E_J. It is possible to perform the required single-qubit operations just by changing the gate voltage.

However, it is desirable to have control over the tunneling amplitude as well. Actually, it is possible to obtain an effective Josephson junction with tunable energy. To do so, the single Josephson junction is replaced by a superconducting loop which is interrupted by two junctions, the so-called superconducting quantum interference device (SQUID). The circuit of such charge qubit is depicted in Fig. 3.5. The loop is also biased by an external flux Φ_{ext}. If the self-inductance of the loop is

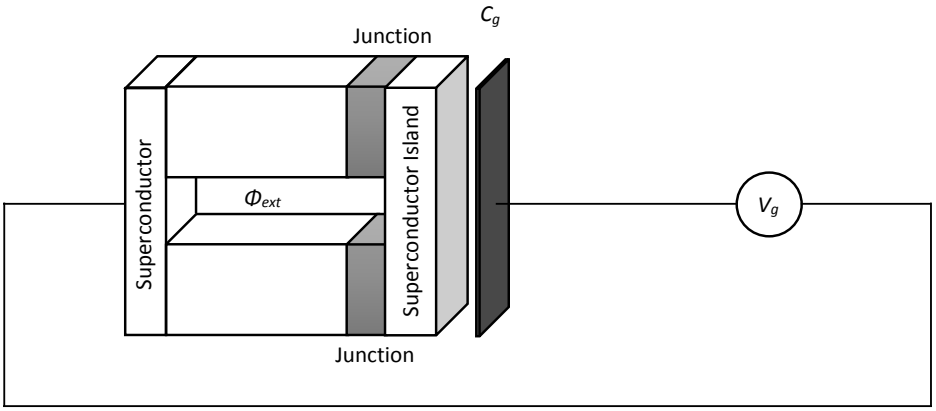

Figure 3.5: A schematic representation of a charge qubit with a SQUID instead of a single junction. In this form of charge qubit the effective Josephson energy is tunable.

low and the two junctions are identical, with the same energy E_J^0, the Hamiltonian of the system takes the same form as of Eq. (3.10) but with the effective Josephson energy for the tunneling amplitude

$$B_x = E_J^{\text{eff}}(\Phi_{\text{ext}}) = 2E_J^0 \cos(\pi \frac{\Phi_{\text{ext}}}{\Phi_0}),$$

which is tunable. The effecting junction capacitance here is the sum of individual capacitance of the two junctions which is $C_J = 2C_J^0$ in the symmetric case.

However, experimentally it cannot be guaranteed with high precision that the two junctions are identical. Therefore the loop is provided with three junctions

that gives the possibility to exactly tune the parameters.

The superconducting charge qubits are very sensitive to the charge noises. It is possible to decrease this sensitivity by slightly changing the corresponding circuit. In the next section the transmon qubit which is more robust against charge noise is introduced.

3.2.1 Transmon Qubit

The charge qubits that are working in the charging regime $E_J/E_C \ll 1$ are sensitive to the charge noise. This is because of the sharp dependency of the charge qubits energy levels to the gate voltage around the degeneracy point $n_g = 1/2$ (see Fig. 3.4). Deviating from the degeneracy point leads to a rapid change in the transition energy between the two levels hence results in a fast dephasing due to the random fluctuations in the gate voltage (confer Eq. 3.11 and 3.12).

The main idea of the transmon qubit is to eliminate this problem by making small the charge dependencies of the energy levels. This can be done by increasing the E_J/E_C ratio as it is shown in Fig. 3.6. The graphs demonstrate the charge qubit three lowest energy levels in terms of the gate voltage n_g for different values of E_J/E_C. The energy levels correspond to the energy spectrum of the Hamiltonian (3.7) with $\hat{n} = -id/d\varphi$. They show that the energy levels become gradually flat as the ratio E_J/E_C increased. A detailed analysis shows that the suppression of the charge sensitivity is exponential in parameter $\sqrt{8E_J/E_C}$.

The only drawback of increasing the ratio E_J/E_C is that it makes the level spectrum to approach that of a harmonic oscillator where the levels are separated by the same energy. However, it can be shown that while the suppression of the charge sensitivity decreases exponentially, the anharmonicity of the levels decreases polynomially with a small power law in E_J/E_C. Therefore, it is possible to greatly reduce the charge sensitivity of the energy levels and simultaneously have sufficiently anharmonicity for the qubit operations.

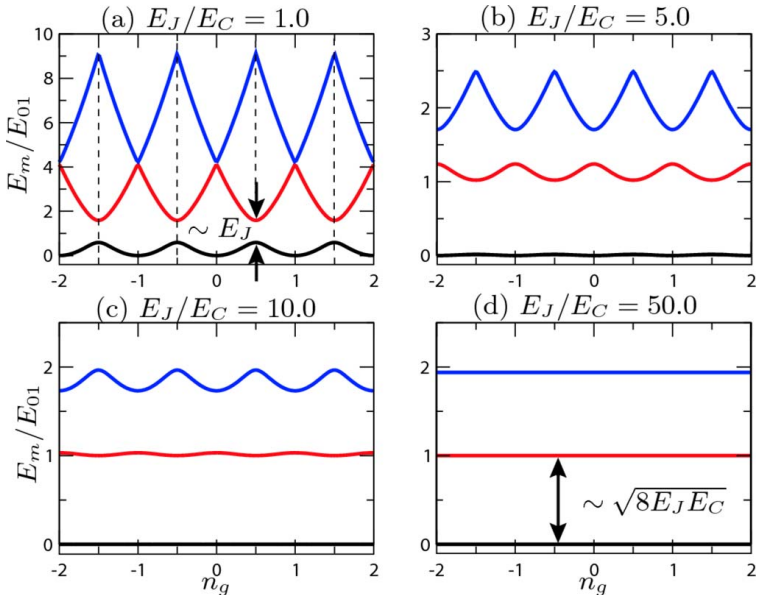

Figure 3.6: Eigenenergies E_m of first three levels ($m = 0, 1, 2$) of the Hamiltonian (3.7) in terms of the charge n_g for different ratios of E_J/E_C in (a) to (d). Energies are given in units of the transition energy E_{01} that is evaluated at the point $n_g = 1/2$. The dashed lines in (a) correspond to the half-integer values of n_g [source: Koch et al. (2007)].

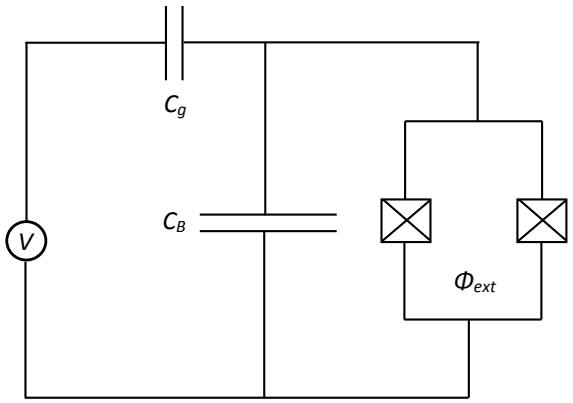

Figure 3.7: Effective circuit diagram of the transmon qubit. The circuit consists of a SQUID that is biased with the flux Φ_{ext} and equipped with an additional large capacitance element C_B.

The circuit of the transmon qubit is shown in Fig. 3.7. The Hamiltonian of

the circuit is given by Eq. (3.7) where the charging energy

$$E_C = \frac{(2e)^2}{2(C_J + C_B + C_g)}$$

can be made small compared to the junction energy by means of the additional capacitance C_B.

In order to control the state of the transmon qubit and performing logic gates, the qubit is embedded in a superconducting transmission line resonator. Such a setup which is called circuit quantum electrodynamics (circuit QED) provides also a system for coupling several transmon qubits to perform multiqubit quantum gates. The next section is devoted to explain the cirquit QED setup.

3.3 Circuit Quantum Electrodynamics

To implement two-qubit gates the pairs of qubit should be coupled together and the interaction between them be controlled. There are various methods to couple the superconducting qubits together. One possibility is to connect the superconducting boxes directly via a capacitor which results in an Ising type interaction term, $\sigma_{kz}\sigma_{lz}$ in the Hamiltonian. Another way is to connect the superconducting circuits in parallel to a common LC oscillator which results in an interaction term of type $\sigma_{ky}\sigma_{ly}$ where the Pauli σ_y is given by

$$\sigma_y = \begin{pmatrix} 0 & -i \\ i & 0 \end{pmatrix}.$$

The method which is discussed here is to couple the superconducting qubits to a single mode of a transmission line resonator. A transmission line resonator is a device where an electromagnetic field is guided along it from one point to another. The length of the transmission line can be much longer than the wavelength of the field that is contained by it. It is possible to model the transmission line resonator by a circuit of infinitely many of infinitesimal LC oscillators. The Hamiltonian of

the transmission line resonator is then proved to be

$$\mathcal{H} = \sum_{n=1}^{\infty} \hbar\omega_n (a_n^\dagger a_n + 1/2). \tag{3.14}$$

Eq. (3.14) is the Hamiltonian of an infinite set of independent harmonic oscillators where $a^\dagger$ and a are creation and annihilation operators, respectively, and ω_n are the frequencies corresponding to the resonator modes. In many situations it is sufficient to keep just a single resonator mode hence the Hamiltonian takes the form

$$\mathcal{H} = \hbar\omega_r (a^\dagger a + 1/2), \tag{3.15}$$

where ω_r is some specified mode frequency.

Figure 3.8 shows the circuit QED architecture. The transmission line resonator consists of a full-wave section of superconducting coplanar waveguides. The superconducting charge qubit is placed between the two superconducting lines and capacitively coupled to the central line where the voltage standing wave is in maximum. In this case the Hamiltonian of the qubit is similar to Eq. 3.8 however the dimensionless gate charge n_g should be replaced by

$$n_g = \frac{C_g}{2e}(V_g^{dc} + \hat{v}) = n_g^{dc} + \frac{C_g}{2e}\hat{v},$$

where V_g^{dc} is the dc part of the voltage and $\hat{v}$ is the quantum part of the voltage due to the resonator. The latter is given by

$$\hat{v} = \sqrt{\frac{\hbar\omega_r}{cL}}(a^\dagger + a),$$

where L is the resonator length and c denotes the capacitance per unit length of the transmission line.

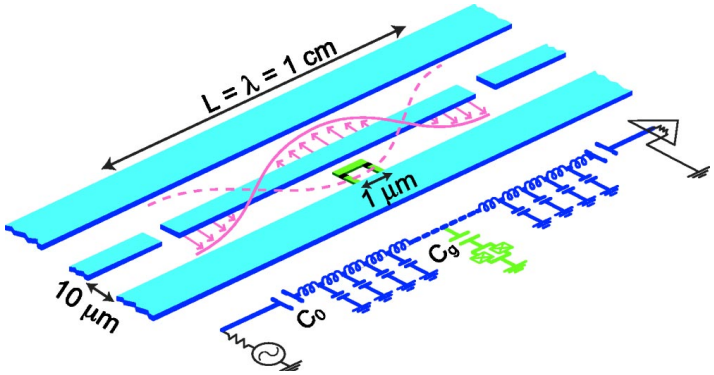

Figure 3.8: Schematic representation of the circuit QED and its equivalent lumped circuit. The transmission line resonator consists of a full-wave section of superconducting coplanar waveguide. The transmon qubit is placed between the superconducting lines and capacitively coupled to the central line where the voltage standing wave is in maximum [source: Blais et al. (2004)].

The total Hamiltonian of the system can then be written as

$$\mathcal{H} = \sum_n \left\{ E_C(n - n_g^{dc} + \frac{C_g}{2e}\hat{v})^2 |n\rangle\langle n| - \frac{1}{2}E_J(|n\rangle\langle n+1| + |n+1\rangle\langle n|) \right\} + \hbar\omega_r a^\dagger a, \tag{3.16}$$

where the second term is the Hamiltonian of the oscillator while neglecting the zero-point energy.

Focusing on $n_g^{dc} \simeq 1/2$ it is possible to keep just the two lowest states, $n = 0, 1$ (see section 3.2). The Hamiltonian (3.16) can be written as

$$\mathcal{H} = -\frac{1}{2}E_C(1 - 2n_g^{dc})\sigma_z - \frac{1}{2}E_J\sigma_x - \frac{eC_g}{(C_g + C_J)}\sqrt{\frac{\hbar\omega_r}{cL}}(a^\dagger + a)(1 - 2n_g^{dc} - \sigma_z) + \hbar\omega_r a^\dagger a, \tag{3.17}$$

where the Pauli matrices are described in terms of the basis $\{|0\rangle, |1\rangle\}$. After rotating the basis to $\{|\uparrow\rangle, |\downarrow\rangle\}$ the Hamiltonian (3.17) takes the form

$$\mathcal{H} = -\frac{1}{2}\hbar\Omega\overline{\sigma_z} - \hbar g(a^\dagger + a)(1 - 2n_g^{dc} - \cos\eta\overline{\sigma_z} + \sin\eta\overline{\sigma_x}) + \hbar\omega_r a^\dagger a, \tag{3.18}$$

where

$$\Omega = \frac{1}{\hbar}\sqrt{E_J^2 + E_C^2(1-2n_g^{dc})^2},$$
$$\eta = \tan^{-1}(E_J/E_C(1-2n_g^{dc}),$$
$$g = \frac{eC_g}{\hbar(C_g+C_J)}\sqrt{\frac{\hbar\omega_r}{cL}},$$

and $\overline{\sigma_z}$ and $\overline{\sigma_x}$ are the Pauli matrices after expressing in terms of the new basis. At the degeneracy point where $n_g^{dc} = 1/2$ ($\eta = \pi/2$) applying the so-called rotating wave approximation reduces the Hamiltonian (3.18) to

$$\mathcal{H} = -\frac{1}{2}\hbar\Omega\sigma_z - \hbar g(a^\dagger\sigma^- + a\sigma^+) + \hbar\omega_r a^\dagger a \tag{3.19}$$

where $\sigma^\pm = (\sigma_x \pm i\sigma_y)/2$ and all the overlines have been dismissed for simplicity. The Hamiltonian (3.19) is the so-called Jayness-Cummings Hamiltonian.

Up to this point it has been described how to couple a qubit to a transmission line resonator. In the rest of this section it is described how to realize single- and multi- qubit operations.

Single qubit gates can be realized by microwaves drive pulses applied on the resonator. A microwave drive can be described by the Hamiltonian

$$\mathcal{H}_d = \varepsilon_d(t)(a^\dagger e^{-i\omega_d t} + a e^{i\omega_d t}) \tag{3.20}$$

where $\varepsilon_d(t)$ is the amplitude and ω_d the frequency of the drive. To see the effect of the drive on the qubit the microwave drive Hamiltonian (3.20) is added to the Hamiltonian (3.19) and the total Hamiltonian is undergone the transformation $U(\mathcal{H}+\mathcal{H}_d)U^\dagger$ with U is given by

$$U = \exp\left[\frac{g}{\Delta}(a\sigma^+ - a^\dagger\sigma^-)\right], \tag{3.21}$$

where $\Delta = \Omega - \omega_r$ is called detuning. For large values of detuning compared to

the coupling g (small values of g/Δ) expanding the transformation to the second order in g/Δ results

$$U(\mathcal{H}+\mathcal{H}_d)U^\dagger \approx \frac{\hbar}{2}[\Omega-\omega_d+2\frac{g^2}{\Delta}(a^\dagger a+\frac{1}{2})]\sigma_z+\hbar\frac{g}{\Delta}\varepsilon_d(t)\sigma_x+ \\ \hbar(\omega_r-\omega_d)a^\dagger a+\hbar\varepsilon_d(t)(a^\dagger+a), \tag{3.22}$$

in a frame rotating at the drive frequency ω_d. Depending on the frequency and amplitude of the drive different quantum gates can be realized.

It is possible to place multiple qubits along the transmission line resonator and implement multiqubit gates. For multiple qubits that are coupled to a transmission line resonator the Hamiltonian takes the form

$$\mathcal{H}=\sum_k -\frac{1}{2}\hbar\Omega_k\sigma_{kz}-\sum_k \hbar g_k(a^\dagger\sigma_k^-+a\sigma_k^+)+\hbar\omega_r a^\dagger a, \tag{3.23}$$

where k runs over the qubits. Considering the transformation

$$U=\exp\left[\sum_k \frac{g_k}{\Delta_k}(a\sigma_k^+-a^\dagger\sigma_k^-)\right], \tag{3.24}$$

with $\Delta_k=\Omega_k-\omega_r$ and applying on the Hamiltonian (3.23) results

$$U\mathcal{H}U^\dagger \approx \hbar\omega_r a^\dagger a+\hbar\sum_k(\Omega_k+\frac{g_k^2}{\Delta_k})\sigma_{kz}+\hbar\sum_k\frac{g_k^2}{\Delta_k}a^\dagger a\sigma_{kz}+ \\ \hbar\sum_{k>l}J_{kl}(\sigma_k^-\sigma_l^++\sigma_k^+\sigma_l^-), \tag{3.25}$$

where

$$J_{kl}=g_k g_l(\frac{1}{\Delta_k}+\frac{1}{\Delta_l}), \tag{3.26}$$

shows an effective coupling between any pairs of the qubits.

The last term in Hamiltonian (3.25) can be written as

$$2\hbar\sum_k J_{kl}(\sigma_{kx}\sigma_{lx}+\sigma_{ky}\sigma_{ly}),$$

which shows an XY type interaction between any pair of the qubits. Evolution of the system under such coupling together with the single qubit manipulation can be used to realize $CNOT$ gate.

However, as it was mentioned in section 2.1.2 it is possible to design microwave drive pulses to realize the multiqubit gates directly. In the next chapter it is described how to design a set of microwave pulses to realize the three qubit Toffoli gate.

Chapter 4

Implementation of the Toffoli Gate in Systems with Imperfections

In this chapter we study the effects of imperfections on the fidelity of the Toffoli gate that can be realized in the circuit QED setup using quantum control methods. The noise is introduced in the interqubits interactions. The coupling constants are no longer fixed, instead, they fluctuate around average values obeying some given probability density functions characterizing the dynamical-imperfection case. We also consider the static-imperfection case in which the values of the coupling constants are not exactly known.

The chapter is organized as follows. section 4.1 is an overview of the quantum control method proposed by Stojanović et al. (2012) to realize a Toffoli gate in the circuit QED setup. The noise model is then described in section 4.2. Sections 4.3 and 4.4 are devoted to analyzing the effects of the dynamical and static noise on the gate fidelity.

4.1 Review of the Implementation of the Toffoli Gate in the Perfect System

In chapter 3 it is described how transmon qubits can be coupled together within circuit QED through a transmission line resonator and controlled through resonant microwave drives. The interaction Hamiltonian of an array of three transmon qubits coupled to a superconducting transmission-line resonator can be effec-

tively described by an XY-type (flip-flop) Hamiltonian

$$H_0 = \sum_{i<j} J_{ij} \left(\sigma_{ix}\sigma_{jx} + \sigma_{iy}\sigma_{jy}\right), \qquad i,j = 1,2,3 \tag{4.1}$$

where J_{ij} are coupling constants and σ_{ix} and σ_{iy} are Pauli X and Y matrices, respectively. This system is manipulated by a Zeeman-like Hamiltonian

$$H_c(t) = \sum_{i=1}^{3} [u_x^{(i)}(t)\sigma_{ix} + u_y^{(i)}(t)\sigma_{iy}], \tag{4.2}$$

with control fields $u_x^{(i)}(t)$ and $u_y^{(i)}(t)$ affecting the qubits in x and y directions. Therefore, the system dynamics is governed by the total Hamiltonian

$$H(t) = H_0 + H_c(t). \tag{4.3}$$

These control fields can be implemented through wave generators. However, to keep the transmon qubits well-defined two-level systems, the fields cannot be arbitrarily large. The norm

$$u_{\max} = \max_{i,t} \sqrt{[u_x^{(i)}(t)]^2 + [u_y^{(i)}(t)]^2} \tag{4.4}$$

is then restricted to be smaller than some threshold value.

The controllability of the system can be verified by considering the Lie algebra generated by span$\{-iH_0, -i\sigma_{jx}, -i\sigma_{jy}; j = 1,2,3\}$ which is actually the Lie algebra $su(8)$. This algebra provides the operator controllability of the system.

Finding the control fields that implement the Toffoli gate is a numerical optimization problem. A given gate time t_g is divided into N_t (even number) intervals of the same time length T. Then, the set of fields is supposed to be constant in each interval and is acting on the related qubits alternating between the x and y directions.

In the first interval $0 \leq t \leq T$, three x-control pulses with constant ampli-

tudes $u_{x,1}^{(i)}$ are applied to all three qubits. The dynamics is then governed by the Hamiltonian

$$H_{x,1} = H_0 + \sum_{i=1}^{3} u_{x,1}^{(i)} \sigma_{ix}. \tag{4.5}$$

In the second interval $T \leq t \leq 2T$, the y-control pulses with amplitudes $u_{y,1}^{(i)}$ are applied leading to the Hamiltonian

$$H_{y,1} = H_0 + \sum_{i=1}^{3} u_{y,1}^{(i)} \sigma_{iy}. \tag{4.6}$$

This process is repeated $N_t/2$ times to complete all N_t intervals. These time-independent Hamiltonians for each interval lead to the time evolution operators

$$U_{x,n} = \exp(-iH_{x,n}T) \tag{4.7}$$

$$U_{y,n} = \exp(-iH_{y,n}T) \tag{4.8}$$

respectively in corresponding intervals, where $n = 1, \ldots, N_t/2$. The product $U_{y,n}U_{x,n}$ in the reverse order, is the time evolution operator $U(t = t_g)$.

The values of the $3N_t$ control fields are obtained through maximizing the fidelity

$$F = \frac{1}{8} \left| \text{ Tr} \left[U^{\dagger} \left(t_g, N_t, \mathbf{u}, \{J_{ij}\} \right) U_{\text{Toff}} \right] \right|, \tag{4.9}$$

where $\mathbf{u}$ is the concatenation of all control pulses and U_{Toff} is the Toffoli gate that is given in Eq. (2.7). The optimized control fields are obtained through numerical maximization of the fidelity with an initial guess for the fields. The minimum gate time for a given fidelity can also be obtained by starting with a sufficiently large t_g and then gradually decreasing its value. The values of N_t and T that are related through $t_g = N_t T$ should be selected such that the corresponding pulse sequence can be generated experimentally.

The piecewise-constant control pulses obtained here can be filtered through a low-pass filter such that they can be generated by an actual wave generator. Using the product formula approach suggested in Heule et al. (2010), it is possible

to obtain the fidelities for the filtered control fields.

Assuming $u_{\max} < 130$ MHz, $J = 30$ MHz and $J_{12} = J_{23} = 6J_{13} = J$, the Toffoli gate can be realized with a fidelity larger than 99% in $4.18J^{-1} = 140$ ns with $N_t = 20$ control intervals. In the following sections we focus on this specific realization.

4.2 Noise Model

In this section we introduce our noise model that is applied to simulate the imperfections in the Toffoli gate implementation. We are specially interested in the case where the interactions between the qubits are noisy. Each J_{ij} in Eq. (4.1) is considered to be independently coupled to a stochastic variable described by

$$J_{ij}(t) = \bar{J}_{ij}\left(1 + \epsilon_{ij}(t)\right), \tag{4.10}$$

where $\bar{J}_{ij}$ are average coupling strengths and $\epsilon_{ij}(t)$ are independent Gaussian random variables for different subindices. This noise model has been used in many physical contexts and can be seen as an effective behavior when we average out the effect of the environment over the main system (Strack and Sachdev, 2011).

We suppose that all $\epsilon_{ij}(t)$ have the same mean and variance and change their values in time simultaneously with a fixed frequency f_c. Then, they remain fixed during the time interval $\tau_c = 1/f_c$:

$$\epsilon(t) = \epsilon^{(k)}, \qquad (k-1)\tau_c \leq t < k\tau_c, \tag{4.11}$$

where we have omitted the subindices because all components have the same behavior. The random variables $\epsilon^{(k)}$ are supposed to be independent and identically distributed (iid) Gaussian random variables in different time intervals with expectation $\mathrm{E}[\epsilon^{(k)}] = 0$ and variance $\mathrm{E}[(\epsilon^{(k)})^2] = \sigma^2 < \infty$, where k runs over integer values.

The autocorrelation function, $R(\tau)$, for $\epsilon(t)$ can be calculated as

$$\begin{aligned} R(\tau) &= \langle \epsilon(t)\epsilon(t+\tau) \rangle \\ &= \lim_{t_M \to \infty} \frac{1}{2t_M} \int_{-t_M}^{+t_M} \epsilon(t)\epsilon(t+\tau)dt \\ &= \lim_{M \to \infty} \frac{1}{2(M\tau_c + \Delta t_M)} \int_{-(M\tau_c+\Delta t_M)}^{+(M\tau_c+\Delta t_M)} \epsilon(t)\epsilon(t+\tau)dt, \end{aligned} \tag{4.12}$$

where t_M can be written as $M\tau_c + \Delta t_M$ with some integer M and $0 \leq \Delta t_M < \tau_c$. Moreover, τ_c is supposed to be finite and different from zero. In order to calculate the last integral in Eq. (4.12), first we note that

$$\int_{(k-1)\tau_c}^{k\tau_c} \epsilon(t)\epsilon(t+\tau)dt = \underbrace{\int_{(k-1)\tau_c}^{k\tau_c-\tau} \epsilon(t)\epsilon(t+\tau)dt}_{I} + \underbrace{\int_{k\tau_c-\tau}^{k\tau_c} \epsilon(t)\epsilon(t+\tau)dt}_{II},$$

where $0 \leq \tau \leq \tau_c$ and the right hand side integrals are calculated as

$$I = \int_{(k-1)\tau_c}^{k\tau_c-\tau} \epsilon^{(k)}\epsilon^{(k)}dt = (\epsilon^{(k)})^2 \int_{(k-1)\tau_c}^{k\tau_c-\tau} dt = (\epsilon^{(k)})^2(\tau_c - \tau),$$

$$II = \int_{k\tau_c-\tau}^{k\tau_c} \epsilon^{(k)}\epsilon^{(k+1)}dt = \epsilon^{(k)}\epsilon^{(k+1)} \int_{k\tau_c-\tau}^{k\tau_c} dt = \epsilon^{(k)}\epsilon^{(k+1)}\tau.$$

Therefore,

$$\begin{aligned} R(\tau) = \lim_{M \to \infty} & \frac{1}{2(M\tau_c + \Delta t_M)} \\ & \left((\tau_c - \tau) \sum_{k=-M}^{M} (\epsilon^{(k)})^2 + \tau \sum_{k=-M}^{M} \epsilon^{(k)}\epsilon^{(k+1)} + Res(\Delta t_M) \right), \end{aligned}$$

where the residual function $Res(\Delta t_M)$ is bounded,

$$Res(\Delta t_M) \leq |(\tau_c - \tau)(\epsilon^{(k)})^2| + |\tau\epsilon^{(k)}\epsilon^{(k+1)}| < \infty.$$

Having performed the same calculations in the case of $-\tau_c \leq \tau \leq 0$ we finally

obtain

$$\langle \epsilon(t)\epsilon(t+\tau)\rangle = \begin{cases} \left(1-\frac{|\tau|}{\tau_c}\right)\sigma^2, & -\tau_c \leq \tau \leq \tau_c \\ 0, & \text{otherwise.} \end{cases} \tag{4.13}$$

The power spectral density (Fourier transform of the autocorrelation function), which displays the essence of the noise, is given by

$$S(\omega) = \frac{\sigma^2\tau_c}{\sqrt{2\pi}}\,\mathrm{sinc}^2\left(\frac{\omega\tau_c}{2}\right). \tag{4.14}$$

In section 4.3 we describe how we simulate the effect of noise on the fidelity for values of τ_c such that $\tau_c \leq t_g$ where t_g is the gate time. For $\tau_c > t_g$ we are only interested in the limit $\tau_c \to \infty$. In this case the power spectral density function approaches to the delta function on zero, which corresponds to a fixed noise in the system. It means that the value of the random variable remains fixed for ever. Physically, this situation is associated with inaccuracies in the system parameters. This situation is analyzed in section 4.4.

4.3 Analyzing the Dynamical Imperfections

Using the noise model introduced in the previous section, we analyze here the implementation of the Toffoli gate when the system is affected by dynamical imperfections. We actually investigate how the gate fidelity is affected by the noise in the system. Then, the system Hamiltonian Eq. (4.1) undergoes noise while the control Hamiltonian Eq. (4.2) is maintained perfect (without noise). The scenario is to apply a set of control fields optimized for the perfect system to an imperfect system. In other words, we analyze the sensitivity of the control fields to the noise in the main system.

We start by obtaining a set of optimal control fields implementing the Toffoli gate in the perfect system. The fields can be found by maximizing the fidelity given by Eq. (4.9) using the parameter values given at the end of section 4.1. To be close enough to the global optimal solution, we carry the maximization process over 200 random initial guesses and then select the set of fields with largest fidelity.

In our noisy system, the couplings J_{ij} in Eq. (4.1) remain no longer fixed and evolve according to Eq. (4.10). There are three different coupling constants and, in principle, the noise affect each of them independently. We are imposing that $\bar{J}_{12} = \bar{J}_{23} = 6\bar{J}_{13} = \bar{J}$ and we are assuming that the random variables $\epsilon_{ij}(t)$ associated with those couplings have the same mean, variance and characteristic frequency. Under those assumptions, we will show later on in this section that introducing the noise only in J is essentially equivalent to introduce the noise in the three coupling constants. This explains why we can drop the subindices of $\epsilon_{ij}(t)$ and call the random variable simply by $\epsilon(t)$.

Let $\epsilon(t)$ change its value with a fixed frequency $f_c = 1/\tau_c$. We generate $t_g f_c$ random numbers independently according to a Gaussian distribution with a zero mean and standard deviation σ. Accordingly, we have a realization of $\epsilon(t)$ as

$$\epsilon(t) = \sum_{k=1}^{t_g f_c} \epsilon^{(k)} \chi_{[(k-1)\tau_c, k\tau_c)} \qquad t \in [0, t_g), \tag{4.15}$$

and therefore $J(t)$ according to Eq. (4.10). The function χ is defined as

$$\chi_{[(k-1)\tau_c, k\tau_c)} = \begin{cases} 1, & t \in [(k-1)\tau_c, k\tau_c) \\ 0, & \text{otherwise.} \end{cases} \tag{4.16}$$

We also set the value of f_c such that the product $t_g f_c$ becomes integer.

It is now possible to calculate the time evolution operator for the noisy system using the total Hamiltonian $H_0(J(t)) + H_c(t)$ with those values of $J(t)$ above realized. Here, we just note that for $T/\tau_c > 1$ each term in Eqs. (4.7) and (4.8) is replaced by a product of exponentials of time-independent Hamiltonians in each τ_c. The corresponding fidelity for that realization can then be calculated using Eq. (4.9).

The next step is to calculate the average fidelity, which is obtained by repeating the above process with the same f_c and σ for a large number of realizations of $\epsilon(t)$ within the corresponding time interval and summing over all fidelities and

dividing by the total number of realizations. Finally, using this method systematically, we obtain the fidelity as a function of σ with a fixed f_c.

Figure 4.1 shows the average fidelity as a function of σ for $t_g f_c = 200, 100, 40, 20, 10, 5, 2, 1$ from top to bottom, respectively. The number of realizations per each fixed σ for the first four items is 10,000 and for the last four items is 100,000. The average fidelity decreases for all frequencies when the standard deviation σ increases, confirming our intuition about the effect of the decoherence over the coherent evolution. Notice that the average fidelity quickly drops to small values specially when $t_g f_c = 5$.

For a given σ, the fidelity is less affected when the noise characteristic frequency is high ($t_g f_c \gg 1$). In other words, the high-frequency noise generates less decoherence. This observation in our simulations can be justified first of all in terms of our noise model specially by looking at the power spectral density given by Eq. (4.14). As the noise frequency increases ($\tau_c \to 0$), the power spectral density function approaches zero for all ω. This means that the noise disappears and the fidelity remains unaffected.

However, an alternative way to analyze this result is using the theorem given by Facchi et al. (2005). The time evolution of the system over each control time $T = \tau_c N$ is given by

$$U_N(T) = \prod_{k=1}^{N} \exp[-i(\bar{H} + \epsilon^{(k)} \bar{H}_0)\tau_c], \tag{4.17}$$

where $\bar{H}_0$ and $\bar{H}$ are obtained from H_0 and H, Eq. (4.1) and Eq. (4.3) respectively, after replacing $\{J_{ij}\}$ by $\{\bar{J}_{ij}\}$. Expanding the product, we can write the result up to the first power of T as

$$1 - i\bar{H}T - \frac{i\bar{H}_0 T}{N} \sum_{k=1}^{N} \epsilon^{(k)}.$$

But according to the weak law of large numbers

$$\lim_{N\to\infty}\left(\left|\frac{1}{N}\sum_{k=1}^{N}\epsilon^{(k)}-E[\epsilon^{(k)}]\right|>\varepsilon\right)=0, \tag{4.18}$$

and thus the first power of $\bar{H}_0 T$ as well as all the higher powers approach zero in probability, hence

$$\lim_{N\to\infty}\left(\parallel U_N(T)-\exp(-i\bar{H}T)\parallel>\varepsilon\right)=0. \tag{4.19}$$

Therefore, the effect of noise disappears if the characteristic frequency τ_c^{-1} is sufficiently high.

The validity of Eq. (4.19) can be also verified by decreasing the number of realizations, that is, performing an average with smaller samples. In this case, the resulting plots will be no longer smooth. Actually, the points in each plot are scattered around the average curve. However, the smoothness of the plots corresponding to high frequencies are less affected. In another words, the plots for higher frequencies are less sensitive to the number of realizations.

However, using the central limit theorem, $\eta=\lim_{N\to\infty}\sum_{k=1}^{N}\epsilon^{(k)}/\sqrt{N}$ goes to a Gaussian distribution with the same mean and variance of $\epsilon^{(k)}$. Therefore, for finite but large N Facchi et al. (2005)

$$U_N(T)\sim\exp(-i\bar{H}T)\exp(-i\eta\bar{H}_0T/\sqrt{N}), \tag{4.20}$$

which shows how the error enters in each control step T of the implementation and the errors will eventually reduce the gate fidelity. This result is not valid for intermediate values of N, since the terms corresponding to the nonzero commutator brackets of $\bar{H}_0$ and $\bar{H}$ become also important.

Figure 4.1 also shows that for a fixed σ the average fidelity decreases when we decrease the noise frequency from $t_g f_c = 200$ until $t_g f_c = 5$ and the fidelity has the opposite behavior from $t_g f_c = 5$ until $t_g f_c = 1$. This behavior can be

explained from the effect of the control pulses on an imperfect system. When the control-pulse frequency is close to the noise frequency, $\tau_c^{-1} = T^{-1}$, its effect helps to protect the system against decoherence, similar to dynamical decoupling Viola et al. (1999); Lidar (2012). When we increase the noise frequency, the control-field effect becomes less relevant, and for $t_g f_c > 5$ it plays almost no role at all.

Finally, Figure 4.1 shows that the curves apparently converge to the same average fidelity for sufficiently large σ. The limiting average fidelity is close to $1/d = 0.125$, which corresponds to the one obtained from the full randomizing map $\varepsilon(\rho) = \mathbb{I}/d$, where ρ is an arbitrary (pure) state and d the Hilbert space dimension. However, this saturation value (0.125) can be obtained if the randomness in the gate parameters uniformly generates all elements in $SU(8)$, and if we end up in a Lie subgroup of $SU(8)$, the saturation value can be different (Heule et al., 2010). What we observe after performing simulations with large values of σ is that the saturation values are not exactly the same, but slightly different depending on the noise frequency. Therefore, fixing the control Hamiltonian and just changing the coupling J does not seem to generate the whole $SU(8)$ space. Figure 4.4 shows the average fidelities for large values of standard deviation.

Now, we come back to justify why introducing one source of noise to J is sufficient to obtain essentially the same results of having three independent sources of noise affecting three couplings $\{J_{12}, J_{13}, J_{23}\}$. In the latter case, the exponent in Eq. (4.17) is replaced by

$$-i(\bar{H} + \boldsymbol{\epsilon}^{(k)} \cdot \bar{\mathbf{H}}_0)\tau_c,$$

where

$$\boldsymbol{\epsilon}^{(k)} = (\epsilon_{12}^{(k)}, \epsilon_{13}^{(k)}, \epsilon_{23}^{(k)}), \tag{4.21}$$

$$\bar{\mathbf{H}}_0 = (H_{12}, H_{13}, H_{23}), \tag{4.22}$$

and

$$H_{ij} = \bar{J}_{ij} \left(\sigma_{ix}\sigma_{jx} + \sigma_{iy}\sigma_{jy} \right), \; i < j. \tag{4.23}$$

By using $\boldsymbol{\eta} = \lim_{N\to\infty} \sum_{k=1}^{N} \boldsymbol{\epsilon}^{(k)}/\sqrt{N}$ instead of η, a similar reasoning to the one used for one J can be applied here to reach the same results as before for high noise frequencies. Moreover, we have repeated the simulations with three independent sources of noise and found essentially the same results for low noise frequencies as well. Figure 4.2 shows the average fidelity as a function of σ in the case of three independent sources of noise. Actually, increasing the number of noise sources just leads to faster decay of average fidelity for all frequencies. Simulations with six different couplings (different couplings in X and Y directions) and with six independent sources of noise confirm the latter statement. Figure 4.3 shows the average fidelity as a function of σ in the case of six independent sources of noise. Moreover, in the new simulations, there is no universal saturation value. Figures 4.5 and 4.6 show the average fidelities for large values of standard deviation in the cases of three and six sources of noise.

4.4 Analyzing the Static Imperfection

As we have discussed at the end of section 4.2, the case $\tau_c \to \infty$ corresponds to a fixed noise in the system, that is, the noise does not change in time. Such a static noise can be associated with, for example, inaccessibility of measuring exactly the system parameters such as the coupling constants. Static noises do not lead to any decoherence, but introduce error into the gate implementation. It is known that entanglement dynamics in similar systems remain almost unchanged under the influence of uniform static noise when it is smaller than 10% (Tsomokos et al. (2007, 2008)).

Analyzing the error for the static-imperfections case is mathematically equivalent to the case of dynamical noise with $\tau_c^{-1} = t_g^{-1}$. Again, we adjust the control Hamiltonian for the perfect system and use it for a system with static imperfections. The coupling is given by Eq. (4.10) with a fixed random variable $\epsilon(t) = \epsilon$ for

the whole evolution. Considering a uniform distribution for ϵ, we generate a large sample of couplings with a given half-width δ and then calculate the corresponding fidelity using Eq. (4.9). After obtaining the sample average and repeating the procedure for many values of δ, we find how the fidelity changes as a function of the half-width. Moreover, we have decreased the noise level interval to be more focused on the region with unaffected entanglement.

Figure 4.7 depicts the average fidelity as a function of the half-width δ. The number of realizations per each fixed δ is 100,000. The diagram shows that the average fidelity decreases when the half-width δ increases. Here, we have focused on half-widths less than 0.5 because the experimental upper bound for such superconducting qubit chain is quite below that (Tsomokos et al., 2007). Actually for disorders such as $\delta \leq 10\%$, the average fidelity remains above 97.83%. Specifically, the fidelity decreases by 2% when the system affected by a uniform noise with half-width less than 10%.

Actually, it is possible to obtain a more robust Toffoli gate that has a better performance while affected by the static uniform noise. In the next chapter we obtain a more robust gate by modifying the quantum optimization problem by using a weighted average of the fidelity over an interval of coupling values as the objective functional.

4.5 Summary and Conclusions

In this chapter we considered the effect of imperfections on a recently established Toffoli gate realized in circuit QED with quantum control methods. The implementation of the gate has been discussed in more details by Stojanović et al. (2012). The total Hamiltonian here is bilinear and we studied the effect of imperfections on the system Hamiltonian by introducing noise in the interqubit couplings. We showed that in the case of dynamical imperfections the average fidelity is less sensitive to noise for high characteristic frequencies. Actually the effect of noise completely disappears when the noise frequency is sufficiently high. For static

noise we showed that the fidelity decreases by 2% when the system affected by a uniform noise with half-width less than 10%. The results in this chapter have been also discussed in (Moqadam et al., 2013) that is recently published in physical review A.

Actually, the results in Stojanović et al. (2012) as well as those were discussed in this chapter are valid under the two-level approximation, i.e., in the absence of any significant leakage from the two-state computational subspace of the transmon qubits. The parameter imperfections studied here can likely be incorporated in an analogous fashion within a more complete multi-level analysis.

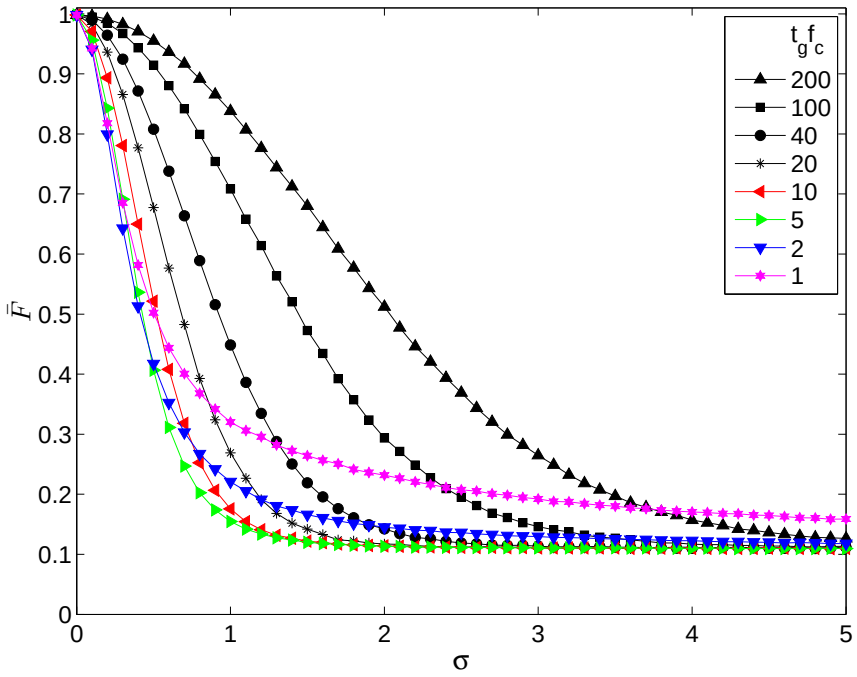

Figure 4.1: The average fidelity versus standard deviation σ for $t_g f_c = 1, 2, 5, 10, 20, 40, 100, 200$. The set of control fields used in each case has been obtained by maximizing Eq. (4.9), which leads to a fidelity about 99.83% with respect to the perfect system.

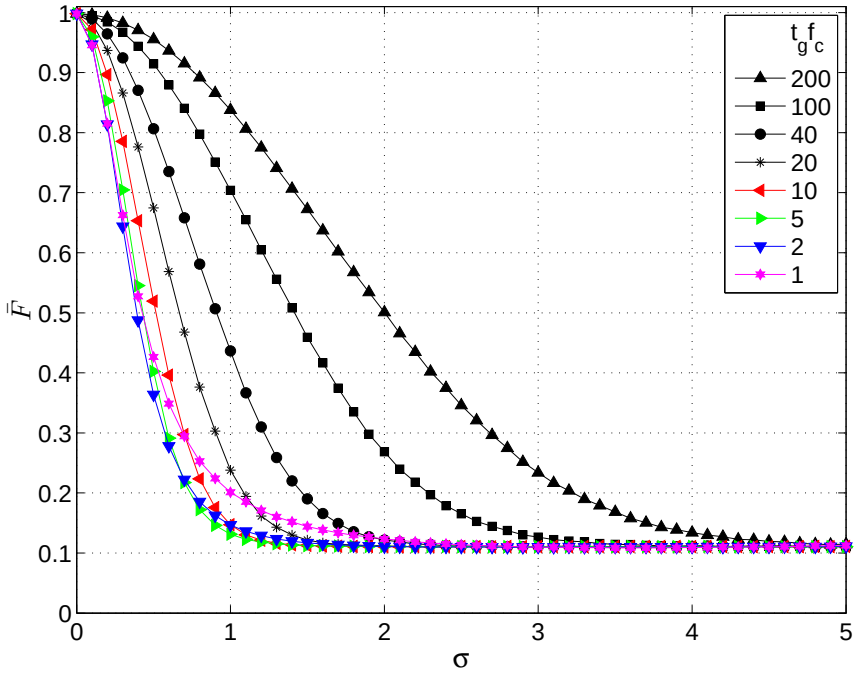

Figure 4.2: The average fidelity versus standard deviation σ in the case of three independent sources of noise for $t_g f_c = 1, 2, 5, 10, 20, 40, 100, 200$. The set of control fields used in each case has been obtained by maximizing Eq. (4.9), which leads to a fidelity about 99.83% with respect to the perfect system.

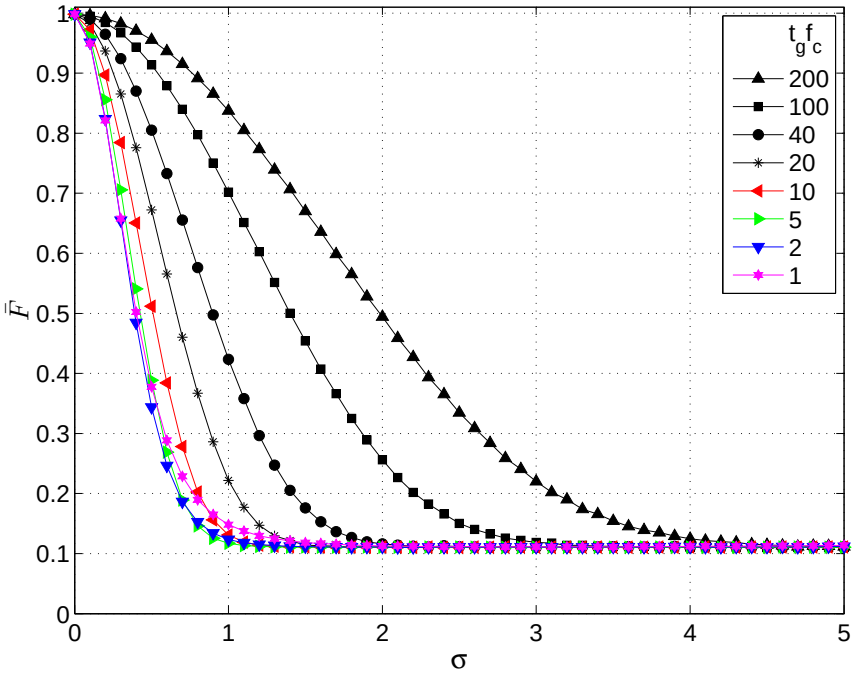

Figure 4.3: The average fidelity versus standard deviation σ in the case of six independent sources of noise for $t_g f_c = 1, 2, 5, 10, 20, 40, 100, 200$. The set of control fields used in each case has been obtained by maximizing Eq. (4.9), which leads to a fidelity about 99.83% with respect to the perfect system.

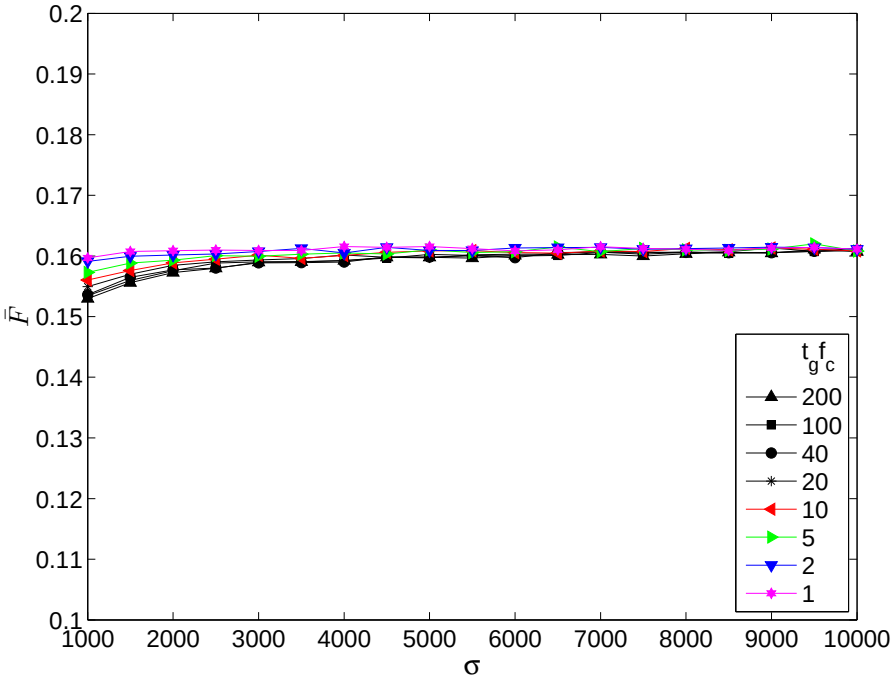

Figure 4.4: The average fidelity versus standard deviation at large values of σ in the case of single source of noise for $t_g f_c = 1, 2, 5, 10, 20, 40, 100, 200$.

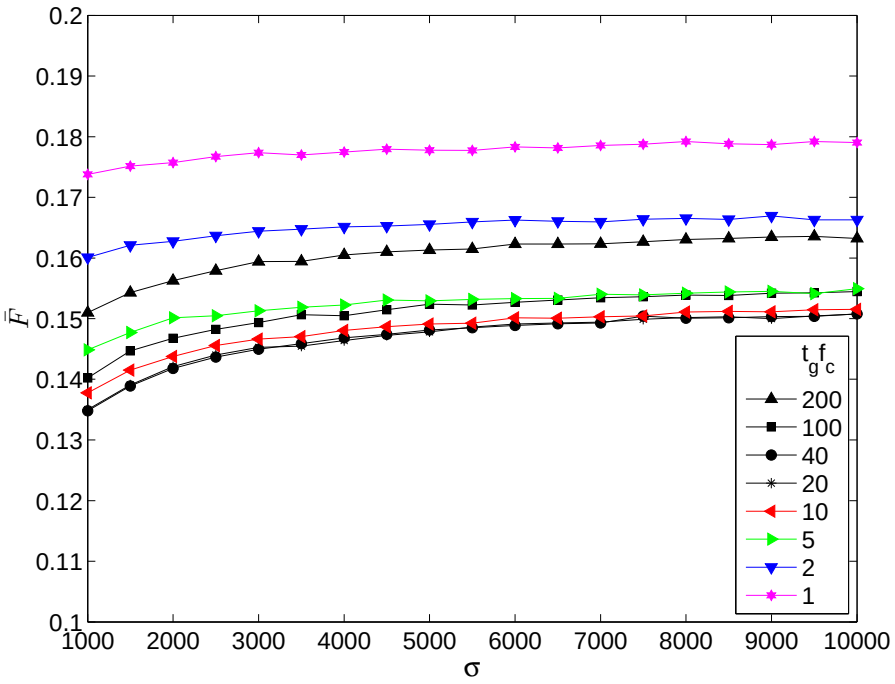

Figure 4.5: The average fidelity versus standard deviation at large values of σ in the case of three sources of noise for $t_g f_c = 1, 2, 5, 10, 20, 40, 100, 200$.

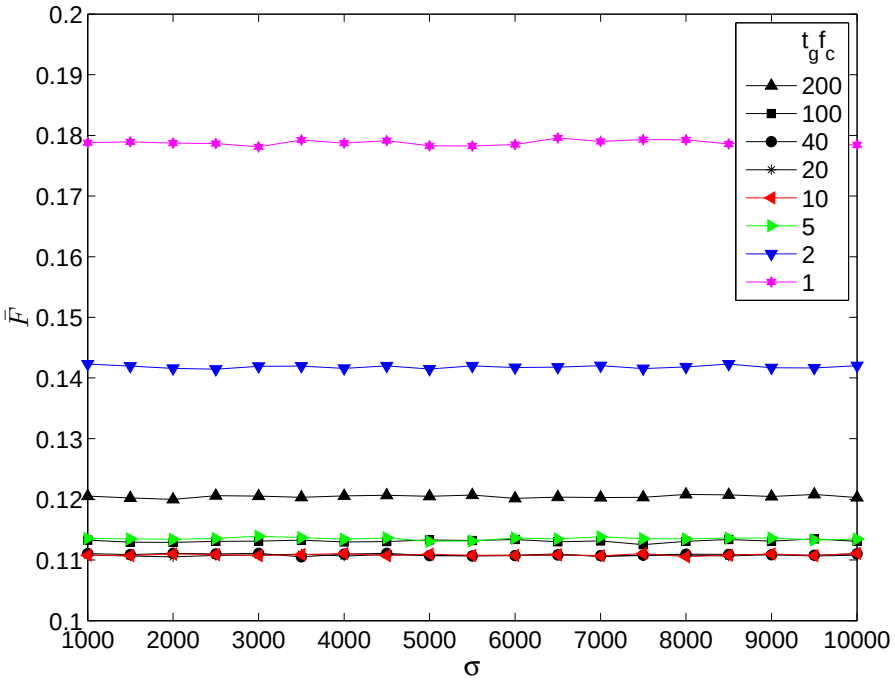

Figure 4.6: The average fidelity versus standard deviation at large values of σ in the case of six sources of noise for $t_g f_c = 1, 2, 5, 10, 20, 40, 100, 200$.

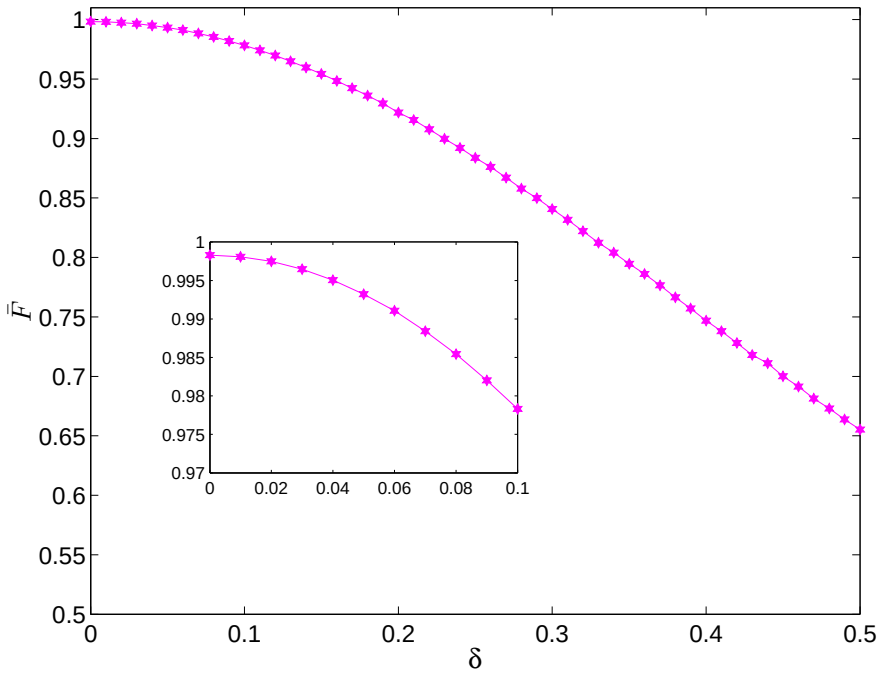

Figure 4.7: The average fidelity versus half-width δ in the case of static imperfections. The set of control fields used here has been obtained by maximizing Eq. (4.9), which leads to a fidelity about 99.83% with respect to the perfect system. Inset: a zoom on the region $0 \leq \delta \leq 0.1$.

Chapter 5

Improving the Gate Fidelity in Systems with Imperfections

In chapter 4, we considered the set of control fields optimized for a fixed value of coupling and then applied that set to a system with imperfections. Actually, we have investigated there the performance of that specific set of fields in the presence of noise. However, it is possible to find other sets of control fields that are more robust to noise. In this chapter, we use the optimal control techniques to find different sets of control fields which yield improved performances in systems with imperfections.

In section 5.1 we find new sets of control fields that maximize a weighted average of the fidelity over a given interval. The performance of the new sets of fields in the presence of noise is analyzed in section 5.2. Finally, in section 5.3 by more manipulating the objective functional we find another set of control fields that are almost insensitive to the noise parameter.

5.1 Optimizing the Weighted Average Fidelity

The set of control fields which is used in chapter 4 is the solution $\mathbf{u}$ of the optimization problem

$$\max_{\mathbf{u}} F\left(\mathbf{u}, \bar{J}\right), \tag{5.1}$$

where F is given by Eq. (4.9). But, the objective functional $F\left(\mathbf{u}, \bar{J}\right)$ uses a single coupling value $J = \bar{J}$, and therefore the resulting optimal solution has the best fidelity at that specific coupling irrespective of the fidelity at points for which $J \neq \bar{J}$. However, with noisy couplings a more robust set of control fields should have high fidelities also in the couplings that deviate from $J = \bar{J}$. To this end, we modify the objective functional such that it includes a range of coupling values $[\bar{J} - \delta J, \bar{J} + \delta J]$. We solve the new optimization problem

$$\max_{\mathbf{u}} \int_{\bar{J}-\delta J}^{\bar{J}+\delta J} F(\mathbf{u}, J) w(J)\, dJ, \tag{5.2}$$

where $w(J)$ is an appropriate weight function enabling us to put different stress on the points in the interval brought into the process of optimization. Actually, the objective functional in problem (5.2) is a weighted average of the fidelity over an interval of coupling values.

The solid line in Figure 5.1 depicts the fidelity in terms of $J/\bar{J}$ for the fields optimized for a single value of coupling $J = \bar{J}$ obtained from solving problem (5.1). Inspired by this plot, we set the weight function such that it has small values in the vicinity of $J/\bar{J} = 1$ and large values in the outermost points of the interval. In fact, by simply letting

$$w(J) = \begin{cases} 0, & \left|\frac{J}{\bar{J}} - 1\right| \leq \delta_1 \\ \\ 1, & \delta_1 < \left|\frac{J}{\bar{J}} - 1\right| \leq \delta_2, \end{cases} \tag{5.3}$$

we can find a new set of control fields leading to higher fidelities in points different from $J/\bar{J}$. Solving the new optimization problem with 200 random initial guesses and choosing the fields with highest fidelity, we can approach to the global solution in this case. The dotted line in Figure 5.1 depicts the corresponding fidelity in terms of $J/\bar{J}$ for such set of fields with $\delta_1 = 0.05$, $\delta_2 = 0.15$, and $\delta J = 0.15\bar{J}$. It can be seen that the new optimal fields, comparing with the previous ones, have smaller

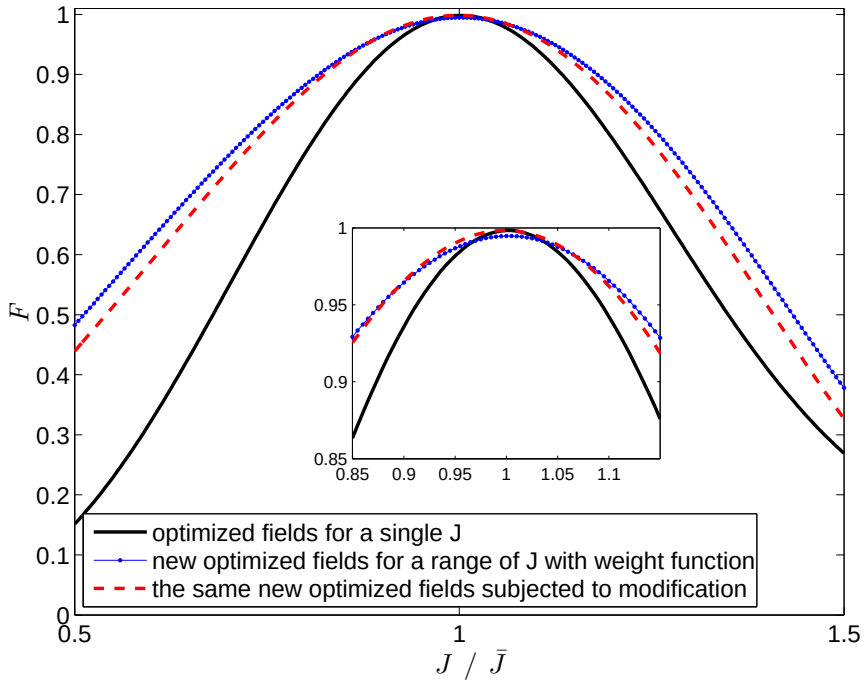

Figure 5.1: Fidelity versus $J/\bar{J}$ for three different sets of control fields: the solid line corresponds to the fields obtained by maximizing Eq. (4.9), the dotted line corresponds to the fields obtained by solving the new optimization problem (5.2) with the weight function (5.3), and the dashed line shows the result by solving the same problem but with the weight function (5.4). Inset: a zoom on the peak.

fidelities in the vicinity of $J/\bar{J} = 1$ but larger in other points.

However, it is possible to improve the fidelities in the vicinity of $J/\bar{J} = 1$, for this new set of optimal fields. We set the weight function as

$$w(J) = F(\mathbf{u}_0, J)^{-1}, \tag{5.4}$$

where $\mathbf{u}_0$ is the set of new optimal fields, i.e., the global solution of the problem (5.2) with the weight function (5.3). The dashed line in Figure 5.1 shows the corresponding fidelity versus $J/\bar{J}$ for such set of fields with $\delta J = 0.1\bar{J}$ and the initial guess equal to $\mathbf{u}_0$. The solid line in Figure 5.1 corresponds to the fields obtained by maximizing Eq. (4.9).

In the next section we analyze the performance of the new sets of control fields obtained here in the presence of imperfections.

5.2 Performance of the New Optimized Sets of Control Fields

In section 4.4 we analyzed the effect of the static imperfection on the fidelity of the Toffoli gate. Having used the same method, In this section we show how the static imperfection affects the fidelity of the gate implemented by the new sets of control fields obtained in section 5.1. In the other words we analyze the robustness of the control fields obtained by optimizing the weighted average fidelity in the presence of static imperfection.

Considering Figure 5.1, we see that the dotted line has the best worst case performance having the largest values at the boundaries $J/\bar{J} = 0.5, 1.5$. However, in the narrower interval $[0.9, 1.1]\bar{J}$ the dotted line and the dashed line have almost the same worst case performance but the dashed line is above the dotted line in a larger part of the interval. As described below, among the three sets of control fields discussed here, the dashed line corresponds to the fields that have the best performance in systems with static disorder less than 10%.

The performance of our new sets of control fields in the presence of noise can be analyzed in the same way of section 4.4. In the case of static imperfections,

the result for the fields optimized according to problem (5.2) with the weight function (5.3) is shown by dotted line in Figure 5.2. The dashed line in the same figure shows the situation for the fields optimized with the weight function (5.4). Specially, for 10% disorder ($\delta = 0.1$) the corresponding fidelities are 98.47% and 98.67%, respectively, showing 0.64% improvement in the first case and 0.84% improvement in the second case, comparing to 97.83% [original problem (5.1)]. The solid line in Figure 5.2 corresponds to the fields obtained in the original problem (5.1) that is the result from section 4.4 repeated here.

For the dynamical-imperfections case, when the noise frequency is high, the resulting plots for the three sets of control fields remain almost the same because the effect of control pulses plays no role in high noise frequencies. However, for low noise frequencies $t_g f_c = 5, 2, 1$ (see section 4.3) the new sets of fields have better performances.

5.3 Stable Toffoli Gate under the Influence of Static Imperfection

In section 5.1, we obtained two new sets of control fields that realize the Toffoli gate with improved average fidelity in the presence of imperfection in the system. The new sets of control fields, comparing to the original set, have more smooth fidelities around the perfect coupling value $J/\bar{J} = 1$ (see Figure 5.1). However, the fidelities can not be completely flat around $J/\bar{J} = 1$. In this section, we modify the original objective functional in a way to obtain a set of control fields having almost fixed fidelity in the interval $|J/\bar{J} - 1| \leq 0.1$.

The desired optimization problem can be written as

$$\begin{aligned} \max_{\mathbf{u}}\{\ & \alpha \left(F(\mathbf{u}, \bar{J} - J_0) + F(\mathbf{u}, \bar{J}) + F(\mathbf{u}, \bar{J} + J_0) \right) \\ & - \beta \left| \, 2F(\mathbf{u}, \bar{J}) - F(\mathbf{u}, \bar{J} - J_0) - F(\mathbf{u}, \bar{J} + J_0) \, \right| \\ & - \gamma \left| \, F(\mathbf{u}, \bar{J} - J_0) - F(\mathbf{u}, \bar{J} + J_0) \, \right| \}, \end{aligned} \tag{5.5}$$

where α, β and γ are some positive constants and J_0 is a point different from

$\bar{J}$. The first term in the optimization problem (5.5) causes the optimized solution has high fidelities in the central point $\bar{J}$ as well as the end points $\bar{J} \pm J_0$. The second term, the sum of distances between the fidelity at the central point and the end points, forces the optimized solution to have a smooth fidelity in the interval $[-J_0, J_0]$. Finally, the last term causes the solution has equal fidelities at the end points.

The solid line in Figure 5.3 shows the fidelity in terms of $J/\bar{J}$ for the fields correspond to the global solution of the optimization problem (5.5) with $\alpha = 1$, $\beta = 10$, $\gamma = 10$ and $J_0 = 0.1\bar{J}$. The set of control fields has been obtained by performing the optimization process over 200 random initial guesses. The corresponding fidelities in the interval $|J/\bar{J} - 1| \leq 0.1$ vary in the range $[0.918, 0.919]$.

The results from the optimizations problem (5.2) with the weight functions (5.3) and (5.4) have also been depicted in Figure 5.3 for comparison. If the set of control fields with the flat fidelity in the interval $|J/\bar{J} - 1| \leq 0.1$ is applied to an imperfect system that has inaccuracy not larger than 10% on the value of J, the fidelity is remained almost constant for any value of imperfection in the interval $0 \leq \delta \leq 0.1$. Hence, although such a set of control fields has not large fidelities at $|J/\bar{J} - 1| \leq 0.1$ it can be considered as a stable realization of the Toffoli gate that is not sensitive to the imperfect parameter.

5.4 Summary and Conclusions

In this chapter, we modified the optimization problem discussed in chapter 4 to obtain new solutions that are more robust in the presence of noise. By optimizing the average fidelity with some special weigh functions, Eqs. (5.3) and (5.4), we obtained new sets of control fields that lead to higher average fidelities in the case of static imperfections. As discussed in chapter 4, the static imperfection with half-width less than 10% half-width causes the average fidelity decrease by 2%. However, the same noise decreases the average fidelities of the new sets of control fields by less than 1.4% and 1.2% in each case, respectively.

Moreover, we obtained another set of control fields that is almost insensitive to static imperfection when the half-width is less than 10%.

Like chapter 4, the results in this chapter are also valid under the two-level approximation, i.e., in the absence of a significant leakage from the two-state computational subspace of the transmon qubits. However, the parameter imperfections studied here can likely be incorporated in an analogous fashion within a more complete multi-level analysis.

The results in Sections 5.1 and 5.2 have been also discussed in (Moqadam et al., 2013) that is recently published in physical review A.

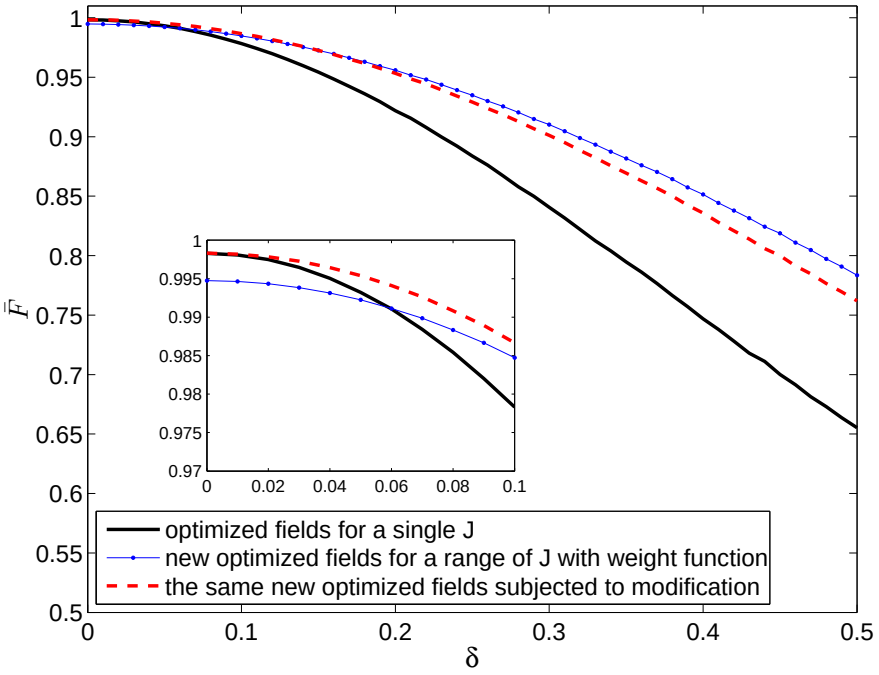

Figure 5.2: The average fidelity versus half-width δ (static imperfections) for three different sets of control fields: the solid line corresponds to the fields obtained by maximizing Eq. (4.9), the dotted line corresponds to the fields obtained by solving the new optimization problem (5.2) with the weight function (5.3) and the dashed line shows the result after solving the same problem but with the weight function (5.4). The corresponding fidelities are about 99.83%, 99.47% and 99.83% for the perfect system, respectively. Inset: a zoom on the region $0 \leq \delta \leq 0.1$.

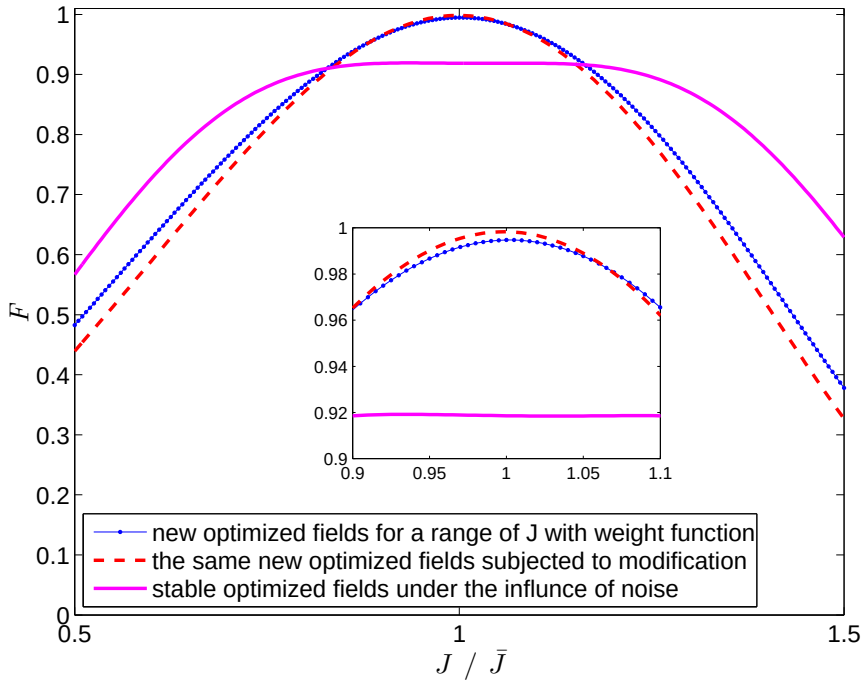

Figure 5.3: Fidelity versus $J/\bar{J}$ for three different sets of control fields: the solid line corresponds to the fields obtained by solving the optimization problem (5.5). The other two plots corresponding to the optimization problem (5.2) with the weight functions (5.3) and (5.4) are repeated from Figure 5.1 for comparison. Inset: a zoom on the peak.

Chapter 6

Summary, Conclusions and Future Works

In this thesis we study the implementation of the Toffoli gate in the systems with imperfections. The Toffoli gate here is realized through application of a sequence of microwave control pulses in a chain of three superconducting charge qubits coupled to a transmission line resonator. For the implementation the transmon qubits have been considered because they are more resistant to the charge noise and have sufficiently large coherence time to realize the gate. The fidelity of the gate in the ideal case is about 99.8%. However, due to the imperfections the fidelity is decreased. We also calculate a new set of microwave control pulses that not only have the same fidelity in the ideal case but also they are more robust to the noise and show an improved performance in the presence of noise.

To simulate the imperfection we introduce the noise in the interqubit interactions in the system. In this way, the coupling values no longer remain fixed hence randomly changes during the time. In the dynamical case, a nonzero frequency is associated to the noise with which the noise realization is changed. We analyze the performance of the set of control pulses that are optimized for the ideal case. To do so, we consider different values for the noise frequency as well as a range of values for the standard deviation of the noise distribution.

According to the numerical simulations, for every value of the noise frequency, the average fidelity of the Toffoli gate is decreased when the standard deviation is

increased. This is in accordance with our intuition about the decoherence over the coherent evolution.

For a fixed value of the standard deviation, the high frequency noises are less dangerous to the system because they generate less decoherence. Actually, when the noise frequency is sufficiently high the effects of the noise disappear and the system dynamics would be similar to the ideal case. Such a behavior can be explained by looking at the noise model that is considered here. The power spectral density when the frequency approaches infinity goes to zero for all frequency components. A more detailed analysis using the law of large numbers shows how the noisy part of the Hamiltonian disappears in the time evolution of the system. Moreover, using the central limit theorem for large but finite noise frequencies shows that how the noise affects the fidelity in each control time interval hence reduces the fidelity.

However, for a fixed value of the standard deviation, the descent of the average fidelity is continued until the noise period becomes 1/5 of the gate time. for noise periods larger than that the average fidelity starts to increase. Considering that the control fields are applied with the period 1/20 of the gate time, we figure out that when the control-field frequency is sufficiently higher than the noise frequency the system is protected against the noise similar to the phenomena of dynamical decoupling.

We also discuss the cases more than one source of noise is introduced to the system. The noise may be appeared independently between the different interqubit couplings and also may be affected independently the coupling values in different directions. However, considering that in our noise model the dynamics of the all noise parameters are similar, the average fidelity dynamics in these cases remain qualitatively similar to the case of single noise source. The average fidelity curves in these cases just decrease faster.

We obtain the average fidelity curves for different values of the noise frequencies for some large values of the standard deviation. Although, as far as we have

simulated, there is no universal value for the fidelities in large standard deviations they remain close to the theoretical value of the full randomizing map saturation value.

After studying the effects of the dynamical noises we also consider the case of static noise. In this case, the noise period is much larger than the gate implementation time. It is associated with a fixed noise in the system. The static noise does not introduce decoherence to the system but does produce error. Using a uniform distribution for the noise it is shown that the average fidelity decreases 2%, when the noise level is less than 10%. Such level of noise is unavoidable in systems that are consisting of superconducting qubits and microwave resonators.

We also use the quantum control techniques to find new sets of control pulses that implement the Toffoli gate with an improved performance in the systems with imperfections. Starting with optimizing a weighted average of the fidelity we obtain a new set of control fields for which the descent of the average fidelity is 1.36% for 10% of the noise level. The new obtained set of control fields has however less fidelity in the ideal case comparing to the original set of fields.

Using an appropriate weight function, we optimize the new set of control fields to obtain another set with high fidelity performance in the ideal case as well. The descent of the average fidelity for this latter set is 1.16%.

Finally, by manipulating the objective functional we find an special set of control fields that is almost insensitive to the noise with half-width less than 10%.

The techniques used in this work may be applied to other multi-qubit gates as well. Specifically, the 2% reduction of the average fidelity could be expected to be also valid for other relevant gates, at least for other three-qubit gates, when the system is affected by a uniform noise with half-width less than 10%.

Moreover, applying the same noise model in a system Hamiltonian written for multi-level qubits (qudits) it is possible to study the effects of the leakage to the higher levels in the system.

Our techniques are also applicable in the problems of pure state controlla-

bility. In this way, it is possible to find the fidelity of the quantum algorithms as well. It may be mentioned that in the quantum algorithms both the operator and state controllability may be used.

We have considered independent distributions in different time intervals for random variables in the noise model Eq. (4.11). It is possible to extend this method simulating other types of noise by considering various dependencies between the random variables in different times. Consequently, the average fidelity may be improved in a more effective way having those sorts of dependencies. As we have experimented, using $1/f$ noise instead of Gaussian noise in different time intervals leads to different behavior of the average fidelity. In this case increasing the noise does not reduces the decoherence. Such situation with $1/f$ noise may be analyzed as well.

Bibliography

Adriano Barenco, Charles H. Bennett, Richard Cleve, David P. DiVincenzo, Norman Margolus, Peter Shor, Tycho Sleator, John A. Smolin, and Harald Weinfurter. Elementary gates for quantum computation. **Phys. Rev. A**, 52:3457, 1995.

Alexandre Blais, Jay Gambetta, A. Wallraff, D. I. Schuster, S. M. Girvin, M. H. Devoret, and R. J. Schoelkopf. Quantum-information processing with circuit quantum electrodynamics. **Phys. Rev. A**, 75:032329, 2007.

Alexandre Blais, Ren-Shou Huang, Andreas Wallraff, SM Girvin, and RJ Schoelkopf. Cavity quantum electrodynamics for superconducting electrical circuits: An architecture for quantum computation. **Physical Review A**, 69(6):062320, 2004.

Y.I. Bogdanov, A.Y. Chernyavskiy, A. Holevo, VF Lukichev, and AA Orlikovsky. Modeling of quantum noise and the quality of hardware components of quantum computers. In: **International Conference on Micro-and Nano-Electronics 2012**, página 87001A. International Society for Optics and Photonics, 2013.

Constantin Brif, Raj Chakrabarti, and Herschel Rabitz. Control of quantum phenomena: past, present and future. **New Journal of Physics**, 12(7):075008, 2010.

Ai Min Chen, Sam Young Cho, and Mun Dae Kim. Implementation of a three-qubit Toffoli gate in a single step. **Phys. Rev. A**, 85:032326, 2012.

John Clarke and Frank K Wilhelm. Superconducting quantum bits. **Nature**, 453 (7198):1031, 2008.

Domenico d'Alessandro. **Introduction to quantum control and dynamics**. Chapman and Hall/CRC,Boca Raton, FL, 2008.

L DiCarlo, JM Chow, JM Gambetta, Lev S Bishop, BR Johnson, DI Schuster, J Majer, A Blais, L Frunzio, SM Girvin, et al. Demonstration of two-qubit algorithms with a superconducting quantum processor. **Nature**, 460(7252):240, 2009.

L DiCarlo, MD Reed, L Sun, BR Johnson, JM Chow, JM Gambetta, L Frunzio, SM Girvin, MH Devoret, and RJ Schoelkopf. Preparation and measurement of three-qubit entanglement in a superconducting circuit. **Nature**, 467(7315):574, 2010.

David P DiVincenzo et al. The physical implementation of quantum computation. **arXiv preprint quant-ph/0002077**, 2000.

Paolo Facchi, Simone Montangero, Rosario Fazio, and Saverio Pascazio. Dynamical imperfections in quantum computers. **Phys. Rev. A**, 71:060306, 2005.

A. Fedorov, L. Steffen, M. Baur, MP da Silva, and A. Wallraff. Implementation of a Toffoli gate with superconducting circuits. **Nature**, 481(7380):170, 2011.

Arkady Fedorov, Lars Steffen, Matthias Baur, MP da Silva, and Andreas Wallraff. Implementation of a Toffoli gate with superconducting circuits. **Nature**, 481 (7380):170, 2012.

B. Georgeot and D. L. Shepelyansky. Emergence of quantum chaos in the quantum computer core and how to manage it. **Phys. Rev. E**, 62:6366, 2000a.

B. Georgeot and D. L. Shepelyansky. Quantum chaos border for quantum computing. **Phys. Rev. E**, 62:3504, 2000b.

Todd Green, Hermann Uys, and Michael J. Biercuk. High-Order Noise Filtering in Nontrivial Quantum Logic Gates. **Phys. Rev. Lett.**, 109:020501, 2012.

Aram W. Harrow and Michael A. Nielsen. Robustness of quantum gates in the presence of noise. **Phys. Rev. A**, 68:012308, 2003.

R. Heule, C. Bruder, D. Burgarth, and V.M. Stojanović. Controlling qubit arrays with anisotropic XXZ Heisenberg interaction by acting on a single qubit. **The European Physical Journal D-Atomic, Molecular, Optical and Plasma Physics**, 63(1):41, 2011.

Rahel Heule, C. Bruder, Daniel Burgarth, and Vladimir M. Stojanović. Local quantum control of Heisenberg spin chains. **Phys. Rev. A**, 82:052333, 2010.

Ryszard Horodecki, Paweł Horodecki, Michał Horodecki, and Karol Horodecki. Quantum entanglement. **Rev. Mod. Phys.**, 81:865, 2009.

Xuedong Hu and S. Das Sarma. Gate errors in solid-state quantum-computer architectures. **Phys. Rev. A**, 66:012312, 2002.

Jens Koch, Terri M. Yu, Jay Gambetta, A. A. Houck, D. I. Schuster, J. Majer, Alexandre Blais, M. H. Devoret, S. M. Girvin, and R. J. Schoelkopf. Charge-insensitive qubit design derived from the Cooper pair box. **Phys. Rev. A**, 76: 042319, 2007.

Peter Lambropoulos and David Petrosyan. **Fundamentals of quantum optics and quantum information**. Springer, 2007.

Michel Le Bellac. **A short introduction to quantum information and quantum computation**. Cambridge university press, 2006.

D.A. Lidar. Review of Decoherence Free Subspaces, Noiseless Subsystems, and Dynamical Decoupling. **arXiv preprint arXiv:1208.5791**, 2012.

S. Machnes, U. Sander, S. J. Glaser, P. de Fouquières, A. Gruslys, S. Schirmer, and T. Schulte-Herbrüggen. Comparing, optimizing, and benchmarking quantum-control algorithms in a unifying programming framework. **Phys. Rev. A**, 84: 022305, 2011.

J Majer, JM Chow, JM Gambetta, Jens Koch, BR Johnson, JA Schreier, L Frunzio, DI Schuster, AA Houck, A Wallraff, et al. Coupling superconducting qubits via a cavity bus. **Nature**, 449(7161):443, 2007.

Yuriy Makhlin, Gerd Schön, and Alexander Shnirman. Quantum-state engineering with Josephson-junction devices. **Rev. Mod. Phys.**, 73:357, 2001.

Simone Montangero, Giuliano Benenti, and Rosario Fazio. Dynamics of Entanglement in Quantum Computers with Imperfections. **Phys. Rev. Lett.**, 91: 187901, 2003.

Simone Montangero and Lorenza Viola. Multipartite entanglement generation and fidelity decay in disordered qubit systems. **Phys. Rev. A**, 73:040302, 2006.

T. Monz, K. Kim, W. Hänsel, M. Riebe, A. S. Villar, P. Schindler, M. Chwalla, M. Hennrich, and R. Blatt. Realization of the Quantum Toffoli Gate with Trapped Ions. **Phys. Rev. Lett.**, 102:040501, 2009.

Jalil Khatibi Moqadam, Renato Portugal, Nami Fux Svaiter, and Gilberto de Oliveira Corrêa. Analyzing the Toffoli gate in disordered circuit QED. **Phys. Rev. A**, 87:042324, 2013.

Michael A Nielsen and Isaac L Chuang. **Quantum computation and quantum information**. Cambridge university press, 2010.

Jorge Nocedal and Stephen J Wright. **Numerical optimization**. Springer, New York, 2nd edition, 2006.

E. Paladino, A. D'Arrigo, A. Mastellone, and G. Falci. Decoherence times of

universal two-qubit gates in the presence of broad-band noise. **New Journal of Physics**, 13(9):093037, 2011.

MD Reed, L. DiCarlo, SE Nigg, L. Sun, L. Frunzio, SM Girvin, and RJ Schoelkopf. Realization of three-qubit quantum error correction with superconducting circuits. **Nature**, 482(7385):382, 2012a.

MD Reed, L DiCarlo, SE Nigg, L Sun, L Frunzio, SM Girvin, and RJ Schoelkopf. Realization of three-qubit quantum error correction with superconducting circuits. **Nature**, 482:382, 2012b.

RJ Schoelkopf, SM Girvin, et al. Wiring up quantum systems. **Nature**, 451(7179): 664, 2008.

Vladimir M. Stojanović, A. Fedorov, A. Wallraff, and C. Bruder. Quantum-control approach to realizing a Toffoli gate in circuit QED. **Phys. Rev. B**, 85:054504, 2012.

Philipp Strack and Subir Sachdev. Dicke Quantum Spin Glass of Atoms and Photons. **Phys. Rev. Lett.**, 107:277202, 2011.

D.I. Tsomokos, S. Ashhab, and F. Nori. Fully connected network of superconducting qubits in a cavity. **New Journal of Physics**, 10(11):113020, 2008.

DI Tsomokos, MJ Hartmann, SF Huelga, and MB Plenio. Entanglement dynamics in chains of qubits with noise and disorder. **New Journal of Physics**, 9(3):79, 2007.

Vlatko Vedral. **Introduction to Quantum Information Science (Oxford Graduate Texts)**. Oxford University Press, Inc., 2006.

Lorenza Viola, Emanuel Knill, and Seth Lloyd. Dynamical Decoupling of Open Quantum Systems. **Phys. Rev. Lett.**, 82:2417, 1999.

JQ You and Franco Nori. Atomic physics and quantum optics using superconducting circuits. **Nature**, 474(7353):589, 2011.